3574 *Organometallics* **1998,** *17,* 3574−3587

# Stereochemical Investigations of the Mechanism of C−H Bond Activation. Diastereomeric and Isotopic Scrambling in (Hydrido)alkyliridium Complexes

T. Andrew Mobley, Christian Schade, and Robert G. Bergman*

*Department of Chemistry, University of California, and the Chemical Sciences Division, Lawrence Berkeley National Laboratory, Berkeley, California 94720-1460*

*Received May 7, 1998*

The diastereomeric complexes (*RS*),(*SR*)-((2,2-dimethylcyclopropyl)(Cp*)($PMe_3$)IrH) (**2a**) and (*RR*),(*SS*)-((2,2-dimethylcyclopropyl)(Cp*)($PMe_3$)IrH) (**2b**) and their α-deuterated analogues (**2a**-$\alpha_{d_1}$, **2b**-$\alpha_{d_1}$) were synthesized in racemic form and separated by low-temperature (−80 °C) column chromatography. Thermolysis (140 °C) of diastereomerically pure **2a** or **2b** in $C_6D_6$ results in its interconversion to the other diastereomer. Thermolysis of the deuterium-labeled analogues **2a**-$\alpha_{d_1}$ and **2b**-$\alpha_{d_1}$ results additionally in scrambling of deuterium from the α-position of the dimethylcylopropyl ring to the metal hydride position. Diastereomer interconversion and isotopic scrambling occur at similar rates, which are faster than the rate observed for the reductive elimination of dimethylcyclopropane and subsequent oxidative addition of $C_6D_6$. Quantitative analysis of these rate data is reported. The similarity of these rates is discussed in terms of a common intermediate mechanism involving a metal alkane (or "σ-alkane") complex. This mechanism is used as a basis for comparison of the rearrangement processes in the current iridium system and the previously reported analogous rhodium system.

## Introduction

Interest in the activation of alkane carbon−hydrogen (C−H) bonds by soluble organometallic complexes is due partly to the potential utility that the selective activation and subsequent functionalization of alkanes would provide the chemical community.[1−3] An important goal for the development of useful alkane C−H bond activation systems is an in-depth understanding of the factors that control the mechanisms (and hence the selectivity) of these reactions. The study described here was motivated by this desire to understand the fundamental nature of the mechanisms of C−H bond activation.

One common mechanism[1,3] for the activation of alkanes is oxidative addition of the C−H bond to an electronically and coordinatively unsaturated transition-metal center (eq 1), resulting in an alkylmetal hydride species. This oxidative addition mechanism for C−H

$$L_nM \xrightarrow{-L} L_{n-1}M \xrightarrow{+RH} L_{n-1}M(R)(H) \qquad (1)$$

activation has been observed and studied intensely by synthetic,[4−16] physical,[17−22] and theoretical techniques,[23−31] resulting in a significant body of work concerning the mechanism by which these reactions occur. Several studies[20,23−25,32−40] have indicated that there may be an intermediate along the reaction path-

---

(1) Arndtsen, B. A.; Bergman, R. G.; Mobley, T. A.; Peterson, T. H. *Acc. Chem. Res.* **1995**, *28*, 154.

(2) (a) Shilov, A. E.; Shul'pin, G. B. *Chem. Rev.* **1997**, *97*, 2879. (b) Crabtree, R. H. *Chem. Rev.* **1985**, *85*, 245.

(3) Hill, C. L. *Activation and Functionalization of Alkanes*; Hill, C. L., Ed.; Wiley: New York, 1989.

(4) Selmeczy, A. D.; Jones, W. D.; Osman, R.; Perutz, R. N. *Organometallics* **1995**, *14*, 5677.

(5) Janowicz, A. H.; Bergman, R. G. *J. Am. Chem. Soc.* **1981**, *103*, 2488.

(6) Hoyano, J. K.; Graham, W. A. G. *J. Am. Chem. Soc.* **1981**, *103*, 3723.

(7) Jones, W. D.; Feher, F. J. *J. Am. Chem. Soc.* **1984**, *106*, 1650.

(8) Jones, W. D.; Feher, F. J. *J. Am. Chem. Soc.* **1986**, *108*, 4814.

(9) Hackett, M.; Ibers, J. A.; Whitesides, G. M. *J. Am. Chem. Soc.* **1988**, *110*, 1436.

(10) Hackett, M.; Whitesides, G. M. *J. Am. Chem. Soc.* **1988**, *110*, 1449.

(11) Gregory, T.; Harper, P.; Shinomoto, R. S.; Deming, M. A.; Flood, T. C. *J. Am. Chem. Soc.* **1988**, *110*, 7915.

(12) Kiel, W. A.; Ball, R. G.; Graham, W. A. G. *J. Organomet. Chem.* **1990**, *383*, 481.

(13) Bergman, R. G.; Seidler, P. F.; Wenzel, T. T. *J. Am. Chem. Soc.* **1985**, *107*, 4358.

(14) Stoutland, P. O.; Bergman, R. G. *J. Am. Chem. Soc.* **1985**, *107*, 4581.

(15) Stoutland, P. O.; Bergman, R. G. *J. Am. Chem. Soc.* **1988**, *110*, 5732.

(16) Purwoko, A. A.; Lees, A. J. *Inorg. Chem.* **1996**, *35*, 675.

(17) Haddleton, D. M.; McCramley, A.; Perutz, R. N. *J. Am. Chem. Soc.* **1988**, *110*, 1810.

(18) Whittlesey, M. K.; Mawby, R. J.; Osman, R.; Perutz, R. N.; Field, L. D.; Wilkinson, M. P.; George, M. W. *J. Am. Chem. Soc.* **1993**, *115*, 8627.

(19) Klassen, J. K.; Selke, M.; Sorensen, A. A.; Yang, G. K. *J. Am. Chem. Soc.* **1990**, *112*, 1267.

(20) Xie, X.; Simon, J. D. *J. Phys. Chem.* **1989**, *93*, 291.

(21) Weiller, B. H.; Wasserman, E. P.; Bergman, R. G.; Moore, C. B.; Pimentel, G. C. *J. Am. Chem. Soc.* **1989**, *111*, 8288.

(22) Bloyce, P. E.; Rest, A. J.; Whitwell, I.; Graham, W. A. G.; Holmes-Smith, R. *J. Chem. Soc., Chem. Commun.* **1988**, 846.

(23) Cundari, T. R. *J. Am. Chem. Soc.* **1994**, *116*, 340.

(24) Song, J.; Hall, M. B. *Organometallics* **1993**, *12*, 3118.

(25) Saillard, J.-L.; Hoffmann, R. *J. Am. Chem. Soc.* **1984**, *106*, 2006.

(26) Jimenez-Catano, R.; Hall, M. B. *Organometallics* **1996**, *15*, 1889.

(27) Siegbahn, P. E. M.; Svensson, M. *J. Am. Chem. Soc.* **1994**, *116*, 10124.

(28) Siegbahn, P. E. M. *J. Am. Chem. Soc.* **1996**, *118*, 1487.

(29) Margl, P.; Ziegler, T.; Blochl, P. E. *J. Am. Chem. Soc.* **1995**, *117*, 12625.

(30) Musaev, D. G.; Morokuma, K. *J. Am. Chem. Soc.* **1995**, *117*, 799.

S0276-7333(98)00355-0 CCC: $15.00

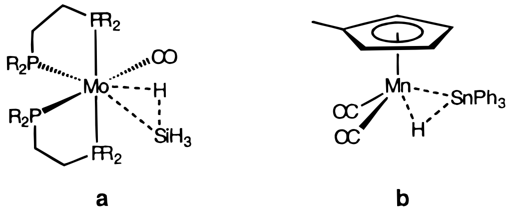

**Figure 1.** Previously determined silane and stannane structures: (a) *cis*-Mo($\eta^2$-SiH$_4$)(CO)(R$_2$PC$_2$H$_4$PR$_2$)$_2$ (R = Ph, *i*-Bu), ref 41; (b) ($\eta^5$-MeC$_5$H$_4$)(CO)$_2$Mn($\eta^2$-HSnPh$_3$), ref 42.

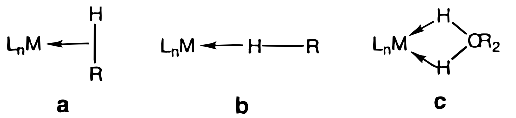

**Figure 2.** Possible structures for alkane complexes: (a) $\eta^2$-C,H side-on interaction, (b) $\eta^1$-H end-on interaction, (c) $\eta^2$-H,H chelated interaction.

way to oxidative addition. This intermediate has been described as a metal complex with the alkane coordinated to the metal center through an intact C−H bond and is often called an alkane complex or a $\sigma$-complex (eq 2).

$$L_nM \xrightarrow{-L} L_{n-1}M \xrightarrow{+RH} L_{n-1}M{\cdot}H{-}R \rightarrow L_{n-1}M(R)(H) \quad (2)$$

No detailed experimental evidence concerning the structure of alkane complexes is available, although they have been detected spectroscopically in gas-phase,[9,10] solution-phase,[18,20,21] and matrix-isolation[17,18,22] experiments. However, metal complexes of heavier congeners of alkanes, silanes[41] and stannanes,[42] have been isolated and fully characterized (Figure 1). These structures, along with the data that have been developed by theoretical studies, allow speculation of possible structures for alkane complexes (Figure 2).

Alkane complexes have been proposed as intermediates in the reactions of several systems pertinent to C−H bond activation. For instance, Bergman,[32,38,39,43] Heinekey,[44] Bercaw,[33] Norton,[34] and Flood[45] have all explained inverse kinetic isotope effects for the reductive elimination of alkanes from metal centers (the microscopic reverse of alkane C−H bond activation by oxidative addition) by the presence of an alkane complex intermediate. Pertinent to the current study, alkane complexes have also been used to explain the scrambling of isotopic labels from the metal hydride to the α-position of metal-bound alkyl groups.[32−34,44] For example,[32] thermolysis of the (deuterio)cyclohexyliridium complex (Cp*)(PMe$_3$)Ir(D)(C$_6$H$_{11}$) results in scrambling of the deuterium from the metal center to the α-carbon (eq 3) at a rate competitive with that of reductive elimination.

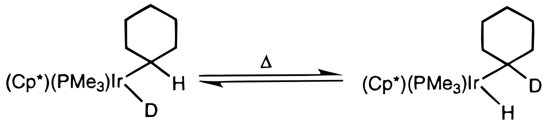

(3)

In a preliminary communication,[46] we described the diastereomeric and isotopic-scrambling processes of two dimethylcyclopropyliridium hydride complexes and proposed the intermediacy of alkane complexes in these transformations. In that communication, we compared the reactivity of the dimethylcyclopropyliridium hydrides with the reactivity of the rhodium analogues previously studied by Periana and Bergman.[43] In the present paper, we report the full details of the synthesis, isolation, and characterization of the dimethylcyclopropyliridium hydride complexes, **2a** and **2b**, and the mechanistic studies of their reactions. A detailed examination of the differences between the kinetics of the iridium and rhodium systems leads to an interesting conclusion concerning the likely structures of alkane complex intermediates.

## Results

**Synthesis of 2a,b.** The synthesis of the diastereomeric complexes **2a,b** was accomplished by two different routes. (1) Photolysis of Cp*(PMe$_3$)IrH$_2$ (**1**) in dimethylcyclopropane (eq 4) results in the loss of dihydrogen and the formation of **2a,b** and **3**. The methyl-activated complex **3** is converted to a 1:1 mixture of the thermodynamically favored cyclopropyl-activated complexes **2a,b** by thermolysis (eq 5) of the mixture in dimethylcyclopropane at 140 °C (2% residual **3**).[47] (2) An alternative synthesis, shown in eqs 6 and 7, allowed us to synthesize **2a,b** as well as their α-deuterio analogues (**2a**-α$_{d_1}$ and **2b**-α$_{d_1}$): treatment of the iridium dibromide

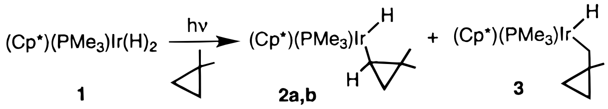

(4)

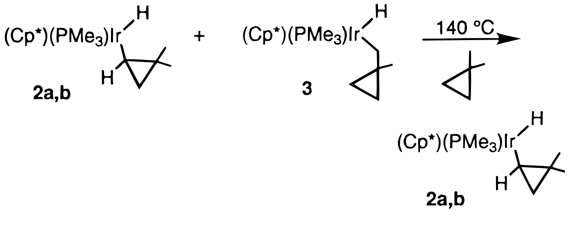

(5)

---

[31] Koga, N.; Morokuma, K. *J. Am. Chem. Soc.* **1993**, *115*, 6883.

[32] Buchanan, J. M.; Stryker, J. M.; Bergman, R. G. *J. Am. Chem. Soc.* **1986**, *108*, 1537.

[33] Parkin, G.; Bercaw, J. E. *Organometallics* **1989**, *8*, 1172.

[34] Bullock, R. M.; Headford, C. E. L.; Hennessy, K. M.; Kegley, S. E.; Norton, J. R. *J. Am. Chem. Soc.* **1989**, *111*, 3897.

[35] Ishikawa, Y.; Brown, C. E.; Hackett, P. A.; Rayner, D. M. *Chem. Phys. Lett.* **1988**, *150*, 506.

[36] Dobson, G. R.; Asali, K. J.; Cate, C. D.; Cate, C. W. *Inorg. Chem.* **1991**, *30*, 4471.

[37] Hop, C. E. C. A.; McMahon, T. B. *J. Am. Chem. Soc.* **1991**, *113*, 355.

[38] Bengali, A. A.; Schultz, R. H.; Moore, C. B.; Bergman, R. G. *J. Am. Chem. Soc.* **1994**, *116*, 9585.

[39] Schultz, R. H.; Bengali, A. A.; Tauber, M. J.; Weiller, B. H.; Wasserman, E. P.; Kyle, K. R.; Moore, C. B.; Bergman, R. G. *J. Am. Chem. Soc.* **1994**, *116*, 7369.

[40] Ziegler, T.; Tschinke, V.; Fan, L.; Becke, A. D. *J. Am. Chem. Soc.* **1989**, *111*, 9177.

[41] Luo, X.-L.; Kubas, G. J.; Burns, C. J.; Bryan, J. C.; Unkefer, C. J. *J. Am. Chem. Soc.* **1995**, *117*, 1159.

[42] Schubert, U.; Kunz, E.; Harkers, B.; Willnecker, J.; Meyer, J. *J. Am. Chem. Soc.* **1989**, *111*, 2572.

[43] Periana, R. A.; Bergman, R. G. *J. Am. Chem. Soc.* **1986**, *108*, 7332.

[44] Heinekey, D. M.; Gould, G. L. *J. Am. Chem. Soc.* **1989**, *111*, 5502.

[45] Wang, C. M.; Ziller, J. W.; Flood, T. C. *J. Am. Chem. Soc.* **1995**, *117*, 1647.

[46] Mobley, T. A.; Schade, C.; Bergman, R. G. *J. Am. Chem. Soc.* **1995**, *117*, 7822.

**Scheme 1**

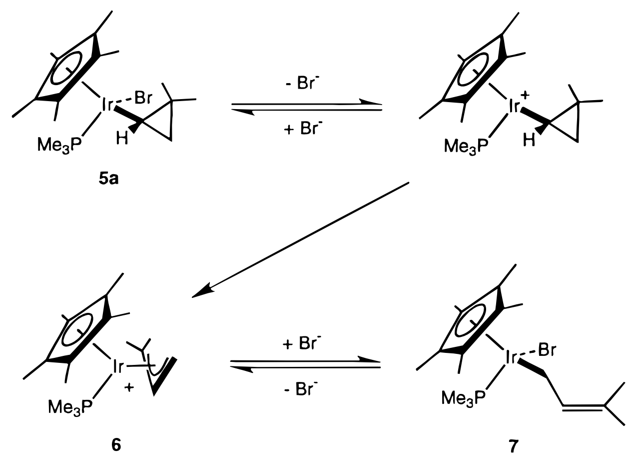

species **4** (generated in situ by the reaction of Cp*(PMe$_3$)-Ir(OTf)$_2$ with LiBr) with an appropriately labeled 1-lithio-2,2-dimethylcyclopropane results in the exclusive formation of the dimethylcyclopropyliridium bromide, **5a**.

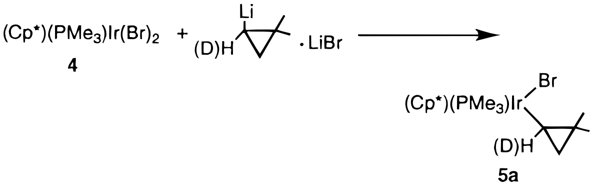

(6)

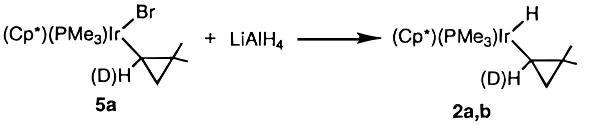

(7)

Upon treatment of **5a** with LiAlH$_4$, both **2a** and **b** are formed in a 1:1 ratio. After workup of the reaction mixture and repeated low-temperature chromatography, **2a** and **2b** (or **2a**-$\alpha_{d_1}$ and **2b**-$\alpha_{d_1}$) are isolated as diastereomerically pure materials (total combined yield of the two diastereomers is 10–15%).

**Synthesis and Reactivity of 5a.** The dimethylcyclopropyliridium bromide complex (*RS*),(*SR*)-(±)-**5a** can be synthesized as a diastereomerically pure material (26% yield) by the reaction shown in eq 6. The other diastereomer, (*RR*),(*SS*)-(±)-**5b**, is not formed in the reaction and is not seen upon thermolysis of **5a** in thf-$d_8$ or $C_6D_6$. Instead, upon thermolysis, **5a** is transformed to the $\eta^1$-allyliridium bromide (±)-**7**. Compound **7** is presumably formed by reaction of the $\eta^3$-$\pi$-allyliridium cation intermediate, **6**, with Br$^-$ as shown in Scheme 1. This ring-opening rearrangement can be inhibited in thf-$d_8$ by the addition of a large amount of dissolved LiBr (50 equiv) to repress Br$^-$ dissociation. Diastereomer **5b** has not, as yet, been observed. Molecular modeling studies of **5a** and **5b** using PC-Model predict that **5a** should lie 3 kcal/mol lower in energy than **5b** (see below).

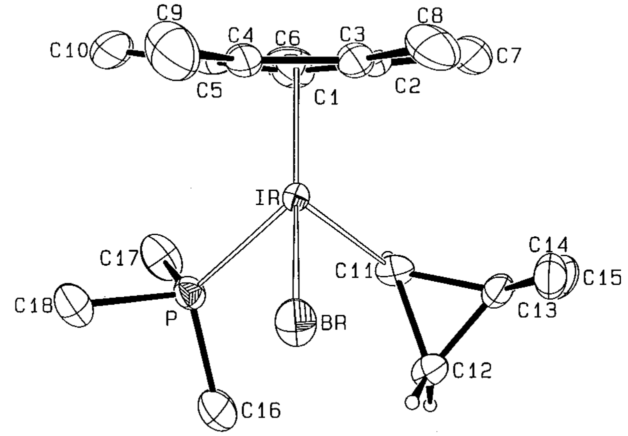

**Figure 3.** ORTEP drawing of (*RS*)-**5a**.

**Table 1. Selected Bond Distances (Å) and Angles (deg) for Complex (*RS*)-(Cp*)(PMe$_3$)Ir(Br)[CHCH$_2$C(CH$_3$)$_2$] (5a)**

| | | | |
|---|---|---|---|
| Ir–Br | 2.553(1) | C(13)–C(14) | 1.505(8) |
| Ir–P | 2.260(1) | C(13)–C(15) | 1.517(9) |
| Ir–C(11) | 2.087(6) | C(11)–H(11) | 0.87(5) |
| C(11)–C(12) | 1.542(8) | C(12)–H(12A) | 1.03(7) |
| C(11)–C(13) | 1.522(8) | C(12)–H(12B) | 0.99(5) |
| C(12)–C(13) | 1.509(8) | | |
| Cp–Ir–Br | 122.61 | Ir–C(11)–C(12) | 128.4(4) |
| Cp–Ir–P | 130.52 | Ir–C(11)–C(13) | 128.2(4) |
| Cp–Ir–C(11) | 123.66 | Ir–C(11)–H(11) | 111.8(31) |
| Br–Ir–P | 86.40(4) | C(12)–C(11)–C(13) | 59.0(4) |
| Br–Ir–C(11) | 95.02(16) | C(11)–C(12)–C(13) | 59.8(4) |
| P–Ir–C(11) | 87.45(17) | C(11)–C(13)–C(12) | 61.2(4) |

**Structure Determination of 5a.** A study of the solid-state and solution-state structures of **5a** was undertaken. Recrystallization of **5a** from toluene/pentane resulted in the formation of crystals suitable for an X-ray diffraction study. An ORTEP drawing of the *RS* isomer of the racemate is shown in Figure 3. Relevant bond distances and bond angles are summarized in Table 1 and crystal and data collection parameters are summarized in Table 2.

The structure of (*RS*),(*SR*)-(±)-**5a** in solution was determined by one- and two-dimensional NMR techniques and agrees with that found for the solid-state structure. The resonances attributed to the protons on the cyclopropyl ring and the methyl groups on the cyclopropyl ring were unambiguously identified using a 2D NOESY experiment (Figure 4). In addition, as seen in the Figure 2, there were additional cross-peaks between the cyclopropyl methylene resonances ($H_{\beta\mathrm{trans}}$ and $H_{\beta\mathrm{cis}}$) and the trimethylphosphine (PMe$_3$) resonance. Similar cross-peaks between the Cp* and the methyls of the cyclopropyl group can also be observed but are much less clear-cut due to $T_1$ noise in the spectrum. This pattern of NOE cross-peaks is consistent with the predicted lowest-energy rotamer of **5a** (see below).

Molecular modeling of complex **5a** was accomplished using the program PC-Model.[48] Initial coordinates for the structure were taken from the Cartesian coordinates of the X-ray crystal structure of **5a**. An energy surface for rotation of the dimethylcyclopropyl group around the Ir–C(11) bond axis was achieved by using a dihedral driver function within the MM2 minimization calcula-

---

(47) To determine whether this represents incomplete reaction or the thermodynamic ratio of **2**/**3** at this temperature, we heated **2a**,**b** at 140 °C in dimethylcyclopropane. Unfortunately, we were not able to detect the expected small amount of **3** by NMR spectrometry before irreversible decomposition began to set in. We therefore cannot rigorously establish that the 98/2 ratio of **2**/**3** represents the equilibrium ratio at this temperature.

(48) Gajewski, J. J.; Gilbert, K. E.; McKelvey, J. *Advances in Molecular Modeling*; JAI Press Inc.: London, 1990; Vol. 2.

**Table 2. Crystal Data for (*RS*)-$(Cp^*)(PMe_3)Ir(Br)[CHCH_2C(CH_3)_2]$ (5a) and $(Cp^*)(PMe_3)Ir(H)[CH_2C(CH_3)C(CH_2)_2]$ (3)**

| | 5a | 3 |
|---|---|---|
| empirical formula | $IrBrPC_{18}H_{33}$ | $IrPC_{15}H_{34}$ |
| temp | −91 °C | −100 °C |
| cryst syst | monoclinic | monoclinic |
| space group | $P2_1/n$ | $P2_1/n$ |
| *a*, Å | 11.144(2) | 13.882(4) |
| *b*, Å | 14.545(2) | 10.424(3) |
| *c*, Å | 12.458(2) | 14.475(3) |
| α, deg | 90.0 | 90.0 |
| *β*, deg | 93.820(13) | 113.08(2) |
| *γ*, deg | 90.0 | 90 |
| *V*, Å$^3$ | 2014.8(9) | 1926.9(22) |
| *Z* | 4 | 4 |
| $D_{calc}$, g cm$^{-3}$ | 1.82 | 1.63 |
| cryst dimens | 0.13 × 0.27 × 0.39 mm | 0.20 × 0.40 × 0.60 |
| *λ*, Å | 0.71073 | 0.71073 |
| $2\theta_{max, deg}$ | 45 | 45 |
| no. of data | 2761 | 2801 |
| no. of unique data ($F^2 > 3\sigma(F^2)$) | 2628 | 2514 |
| no. of variables | 323 | 181 |
| *R* | 2.15% | 3.5% |
| $R_w$ | 2.57% | 4.4% |
| $R_{all}$ | 2.83% | 4.5% |
| GOF | 1.33 | 1.47 |

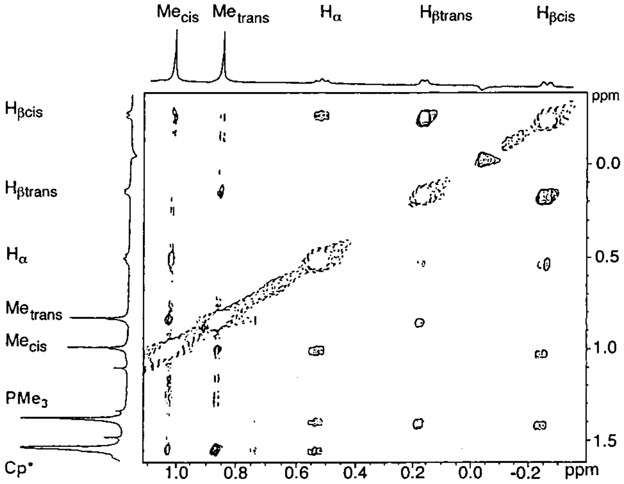

**Figure 4.** $^1H\{^{31}P\}$ NOESY spectrum of (*RS*),(*SR*)-(±)-**5a** in THF-*d*8. The diagonal peaks are shown as positive (broken lines).

tion. The plot of energy vs dihedral angle (C(12)−C(11)−Ir−Br) is provided as Supporting Information. Further minimizations were carried out on the local minima found on this energy surface with full freedom of motion for the previously constrained dihedral angle. Rotation around the C(11)−Ir bond results in higher energy structures (all local minima resulted in ≥3 kcal/mol increase in energy). A Schakal drawing of the minimized lowest energy structure of **5a** is shown in Figure 5. We conclude that the NOESY data reflect the dipole−dipole relaxation interactions present in the lowest energy rotamer and that the structure of **5a** in solution is similar to that in the solid state.

Studies on the second diastereomer, **5b**, were carried out similarly. The lowest energy rotamer for **5b** was 4 kcal/mol higher in energy than the lowest energy rotamer for **5a**.

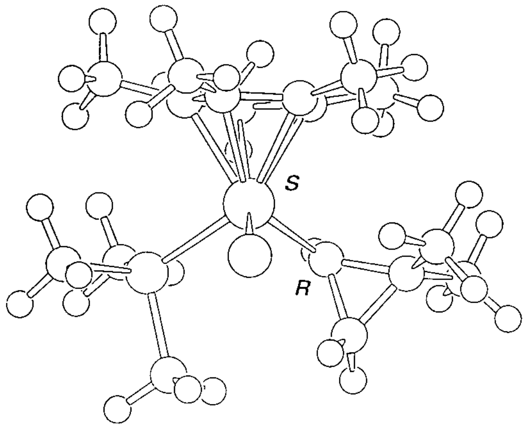

**Figure 5.** Rotamer of **5a** responsible for dipole−dipole relaxation interactions observed in the NOESY spectrum shown in Figure 4. The structure was determined by MM2 minimization using PC-Model (v.5) and drawn using Schakal-92.

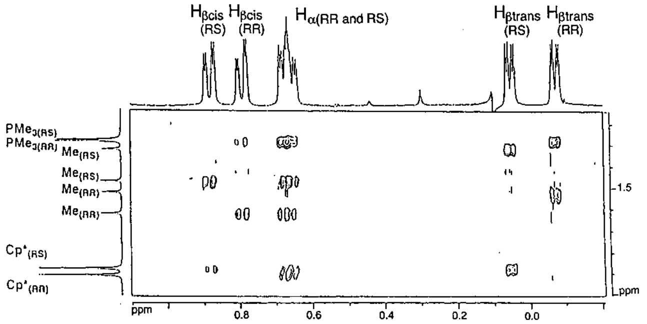

**Figure 6.** $^1H\{^{31}P\}$ NOESY spectrum of (±)-**2a,b** in $C_6D_6$.

**Structure Determination of 2a,b.** Crystals of sufficient quality for an X-ray structure determination of **2a** or **2b** could not be obtained; however, the structures of **2a** and **2b** were determined using one- and two-dimensional NMR techniques. The resonances attributed to the protons on the cyclopropyl ring and the protons of the methyl groups on the cyclopropyl ring were identified for **2a** and **2b** by analyzing a 2D NOESY experiment performed on a 1:1 mixture of **2a,b** (Figure 6). Similar to **5a**, complex **2a** shows NOESY cross-peaks between the cyclopropyl methylene resonances and the $PMe_3$ resonance. Conversely, **2b** shows NOESY cross-peaks between the cyclopropyl methylene resonances and the methyl resonance of the pentamethylcyclopentadienyl (Cp*) group. This pattern of cross-peaks for **2a** and **2b** and the similarity of the cross-peaks for **2a** and structurally known **5a** lead us to assign **2a** as the (*RR*),(*SS*) diastereomeric pair of enantiomers and **2b** as the (*RS*),(*SR*) diastereomeric pair of enantiomers as pictured in Figure 7. Molecular modeling of complexes **2a** and **2b** was accomplished in a manner similar to that described above for **5a,b**. Schakal stereodrawings of the minimized structures for **2a** and **2b** are shown in Figure 7.

**Independent Synthesis and X-ray Crystallographic Characterization of 3.** Methyl-activated complex **3** was independently synthesized by reaction of $(Cp^*)(PMe_3)Ir(Li)(H)$ with (1-methylcyclopropyl)methyl tosylate (eq 8). Low-temperature (−80 °C) chroma-

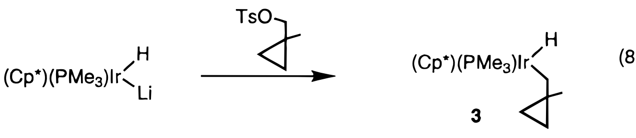

(8)

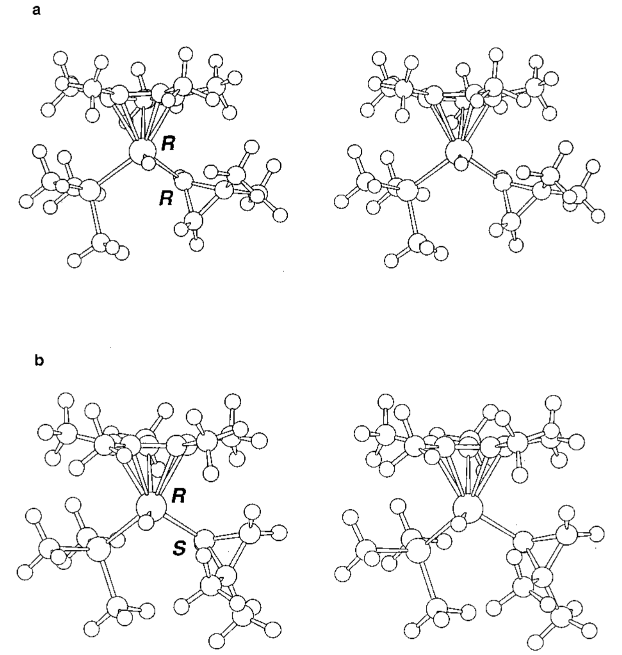

**Figure 7.** Stereoscopic drawings of the rotamers of (*RR*)-**2a** and (*RS*)-**2b** responsible for dipole–dipole relaxation interactions observed in the 2D NOESY spectrum shown in Figure 6. The structures were determined by MM2 minimization using PC-Model (v.5) and drawn using Schakal-92.

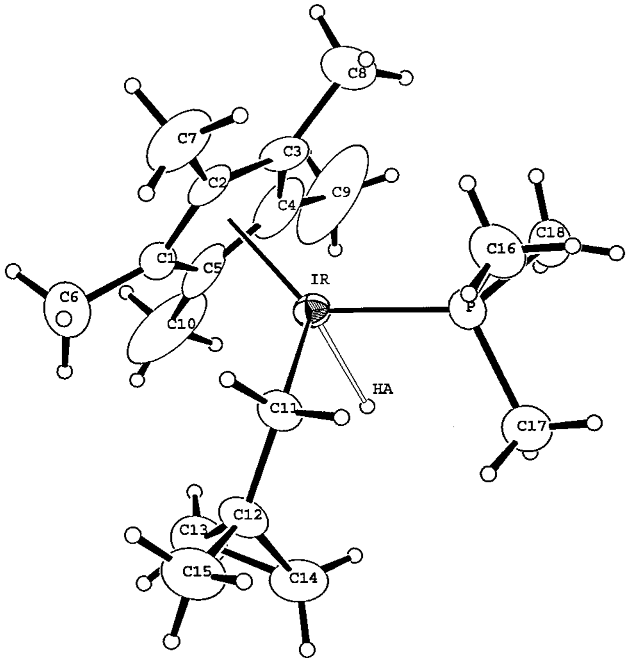

**Figure 8.** ORTEP drawing of **3**.

**Table 3. Selected Bond Distances (Å) and Angles (deg) for Complex (Cp*)(PMe$_3$)Ir(H)[CH$_2$C(CH$_3$)C(CH$_2$)$_2$] (3)**

| | | | |
|---|---|---|---|
| Ir–Ha | 1.770(1) | C(12)–C(14) | 1.482(9) |
| Ir–P | 2.217(2) | C(12)–C(13) | 1.498(11) |
| Ir–C(11) | 2.116(7) | C(13)–C(14) | 1.515(12) |
| C(11)–C(12) | 1.523(9) | C(12)–C(15) | 1.511(11) |
| Ha–Ir–P | 74.84(5) | C(13)–C(12)–C(14) | 61.1(5) |
| Ha–Ir–C(11) | 88.09(18) | C(12)–C(13)–C(14) | 58.9(5) |
| P–Ir–C(11) | 86.84(21) | C(12)–C(14)–C(13) | 60.0(5) |
| Ir–C(11)–C(12) | 122.0(5) | C(11)–C(12)–C(15) | 112.3(6) |

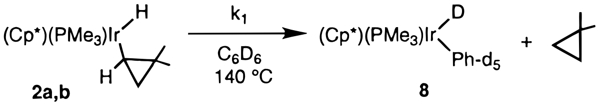

(9)

tography on alumina III and recrystallization from methylcyclohexane at −40 °C gave X-ray quality crystals. An ORTEP drawing of the crystal structure is given in Figure 8, and selected bond distances and angles are summarized in Table 3. Crystal and data collection parameters are summarized in Table 2.

**Kinetic Study of the Thermolysis of 2a,b.** To gain information regarding the mechanism of the reductive elimination of dimethylcyclopropane from **2a,b**, a kinetic study was undertaken. The overall reaction observed is shown in eq 9. Thermolysis of a mixture of **2a,b** at 140 °C in $C_6D_6$ leads to reductive elimination of dimethylcyclopropane and oxidative addition of $C_6D_6$ to produce the pentadeuteriophenyliridium deuteride (**8**). The time dependence of the disappearance of the Cp* and PMe$_3$ $^1$H NMR resonances of **2a,b** could be fit to a pseudo-first-order rate law (eq 10) with a rate constant[49] of $k_1 = (1.8 \pm 0.8) \times 10^{-6}\ s^{-1}$. Starting with a 1:1 mixture of

$$\frac{-d[\mathbf{2a,b}]}{dt} = k_1[\mathbf{2a,b}] \tag{10}$$

**2a** and **2b**, the ratio of **2a**:**2b** does not change during the course of the thermolysis.

The chromatographic separation of **2a** and **2b** allowed us to carry out the thermolysis experiments using the pure diastereomers. Upon thermolysis of either diastereomer at 140 °C, in addition to the reductive elimination process described above, the starting diastereomer is converted to its isomer (eq 11) at a rate that is faster than that of full reductive elimination and oxidative addition (eq 9). The diastereomer interconversion could be followed by observing the cyclopropylmethylene, cyclopropylmethyl, and metal hydride $^1$H NMR resonances and the $^{31}P\{^1H\}$ resonances for the two complexes. A plot of the integrated region of any of these resonances vs time of thermolysis results in a biexponential curve. A representative plot of the experimental data is shown in Figure 9.

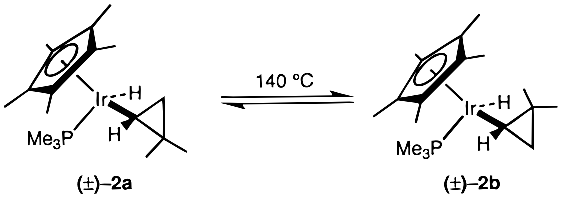

(11)

A quantitative analysis of these data was carried out using two computer programs[50] to perform a nonlinear regression with least-squares fitting of the experimental data. The two kinetic models A and B, depicted in Scheme 2, were explored. A detailed explanation of the

---

(49) The rate constant $k_1$ was determined by thermolysis of a 1:1 mixture of **2a**,**b** in $C_6D_6$.

(50) Three Fortran programs were used to fit the data using numerical integration and least-squares nonlinear regression: Gear (v. 2.1) and Git (v. 2.1) were written by R. J. McKinney and F. J. Weigert at E. I. DuPont & Nemours Co., and Calkinetics (v. 1.0) was written by J. Krom (currently at Cornell University). The results obtained using Gear and Git agreed with those using Calkinetics.

**Scheme 2**

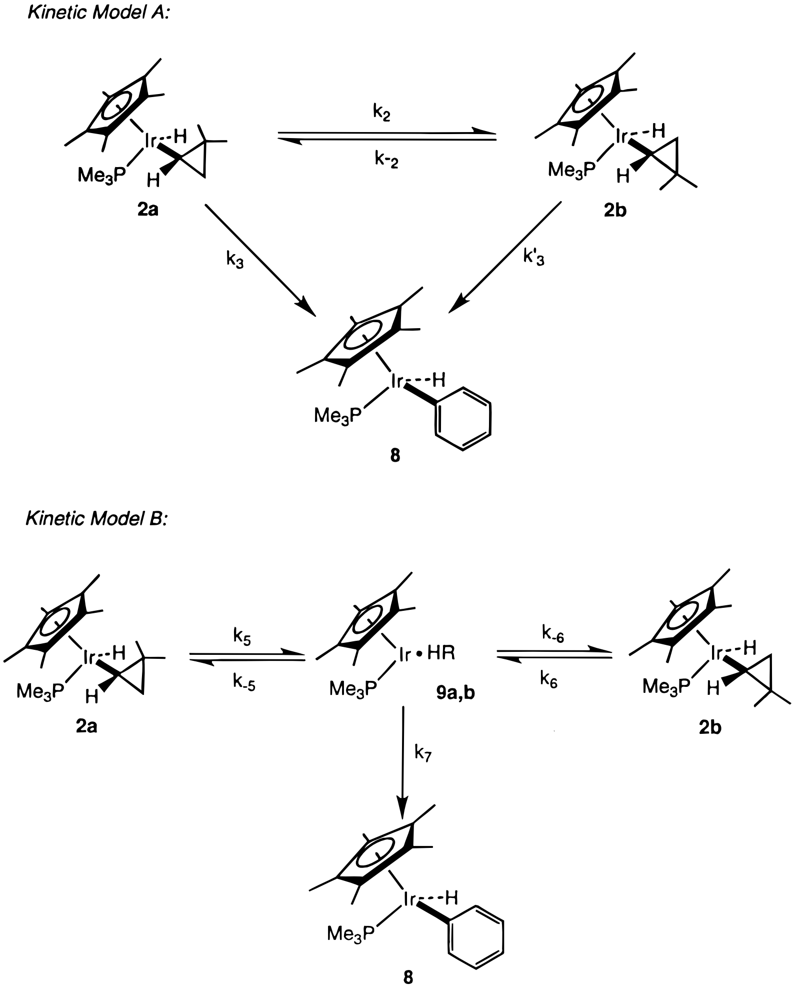

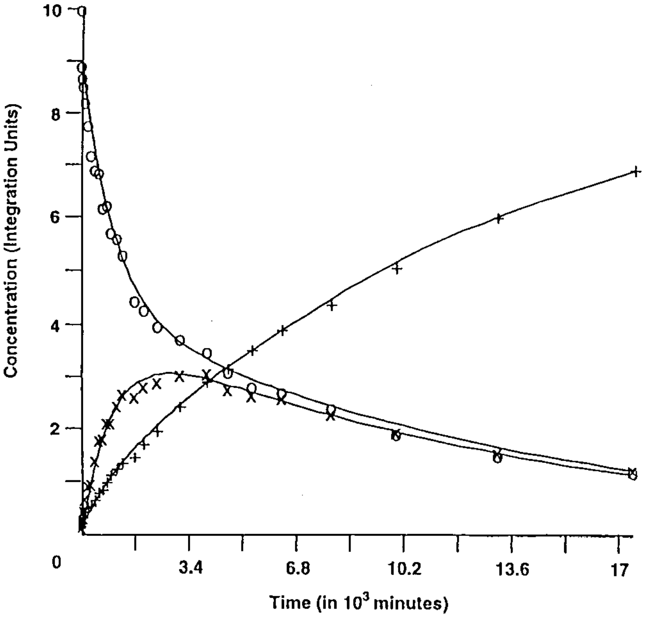

**Figure 9.** Representative plot of the kinetic data for the thermolysis of (*RR*),(*SS*)-(±)-**2a** (○), (*RS*),(*SR*)-(±)-**2b** (×), and **8** (+) in $C_6D_6$. The curves are nonlinear regression least-squares best fits of the experimental data determined using kinetic model A.

**Table 4. Rate Constants for Kinetics of Diastereomer Interconversion, Deuterium Scrambling, and Reductive Elimination from (*RR*),(*SS*)-(±)-2a, (*RS*),(*SR*)-(±)-2b, (*RR*),(*SS*)-(±)-2a-$\alpha_{d_1}$, (*RS*),(*SR*)-(±)-2b-$\alpha_{d_1}$**

Rate Constants for the Reductive Elimination of **2a**,**b**

$k_1 = (1.8 \pm 0.8) \times 10^{-6}\ s^{-1}$

Rate Constants from Least-Squares Fits to Kinetic Model A

$k_2 = (7.3 \pm 1.2) \times 10^{-6}\ s^{-1}$

$k_{-2} = (6.8 \pm 0.7) \times 10^{-6}\ s^{-1}$

$k_3 + k_{3'} = (2.3 \pm 0.8) \times 10^{-6}\ s^{-1}$

Rate Constants from Least-Squares Fits to Kinetic Model B

$k_5 = (8.7 \pm 1.0) \times 10^{-6}\ s^{-1}$

$k_6 = (1.1 \pm 0.2) \times 10^{-4}\ s^{-1}$

$k_{-6}/k_{-5} = 14.9 \pm 2.8$

$k_7/k_{-5} = 0.35 \pm 0.04$

Rate Constants and Equilibrium Constants from Deuterium-Scrambling Process

$K_{eqHD} = 0.47 \pm 0.03$

$k_{obsHD} = 1.6 \pm 0.1 \times 10^{-5}\ s^{-1}$

$k_4 = (5.2 \pm 2.8) \times 10^{-6}\ s^{-1}$

$k_{-4} = (1.1 \pm 0.1) \times 10^{-5}\ s^{-1}$

analytical process, including derivation of the rate equations for both models, is given as Supporting Information. Figure 9 shows a representative fit to the experimental data.

Fitting the data to kinetic model A yields the phenomenological rate constants for the system; rate data derived from the fitting of model A to several kinetic trials are summarized in Table 4. The phenomenological rate constants for the interconversion of **2a** and **2b** ($k_2$ and $k_{-2}$) are the same within experimental error and

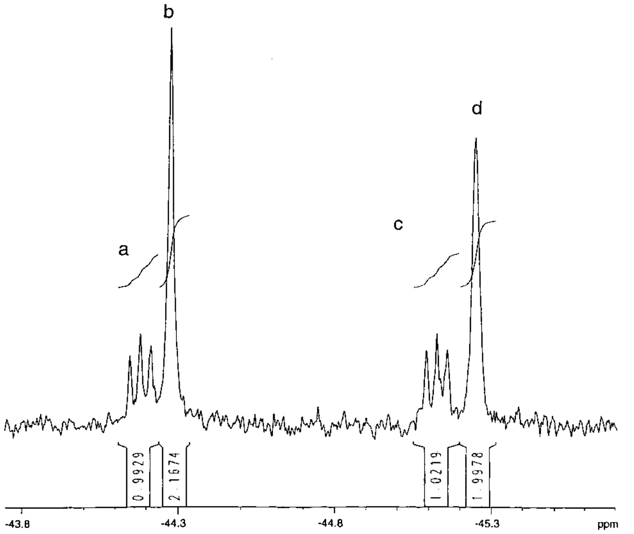

**Figure 10.** $^{31}P\{^1H\}$ NMR spectrum: (a) **2a**-hyd$_{d_1}$, (b) **2a**-$\alpha_{d_1}$, (c) **2b**-hyd$_{d_1}$, (d) **2b**-$\alpha_{d_1}$.

are approximately 3 times faster than $k_3$ and $k_{3'}$, the rate constants for formation of **8**. The latter rate constants determined by the nonlinear least-squares regression analysis agree well with that determined by thermolysis of the 1:1 mixture of **2a,b**. Fitting the data to kinetic model B yields the rate constants summarized in Table 4.

**Thermolysis of 2a,b-$\alpha_{d_1}$.** Thermolysis of diastereomerically pure deuterium-labeled (±)-**2a**-$\alpha_{d_1}$ (or (±)-**2b**-$\alpha_{d_1}$) results in (1) the scrambling of the deuterium from the α-position of the dimethylcyclopropyl ring to the metal hydride position to generate (±)-**2a**-hyd$_{d_1}$ (or (±)-**2b**-hyd$_{d_1}$) and (2) conversion to the other diastereomer, (±)-**2b**-$\alpha_{d_1}$ and (±)-**2b**-hyd$_{d_1}$ (or (±)-**2a**-$\alpha_{d_1}$ and (±)-**2a**-hyd$_{d_1}$) (eq 12). Deuterium scrambling was evidenced by a decrease in the integration of the hydride resonance and the appearance of the α-proton resonance in the $^1$H NMR spectrum, the appearance of deuterium-coupled, isotopically shifted $PMe_3$ resonances ($J_{P-D}$ = 5 Hz) in the $^{31}P\{^1H\}$ NMR spectrum (Figure 10), and the appearance of metal deuteride resonances ($J_{P-D}$ = 4 Hz) in the $^2H\{^1H\}$ NMR spectrum (Figure 11). At extended thermolysis times, four small resonances attributable to the methylene resonances (**2a**-$\beta_{cis}$, **2a**-$\beta_{trans}$, **2b**-$\beta_{cis}$, and **2b**-$\beta_{trans}$) of **2a** and **2b** were also detected in the $^2H\{^1H\}$ NMR spectrum (relative intensity 1:1:1:1).

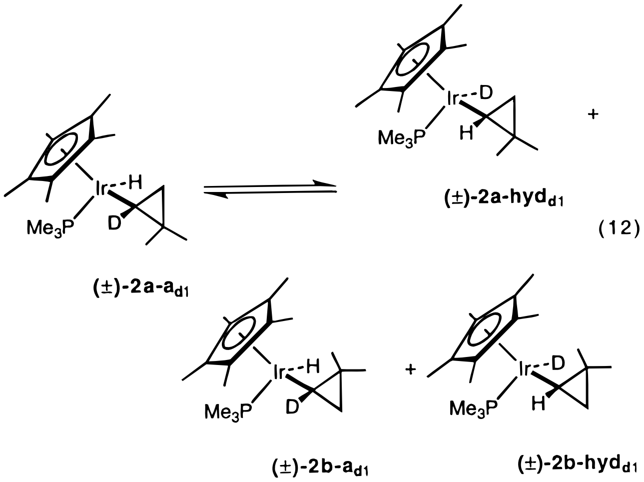

(12)

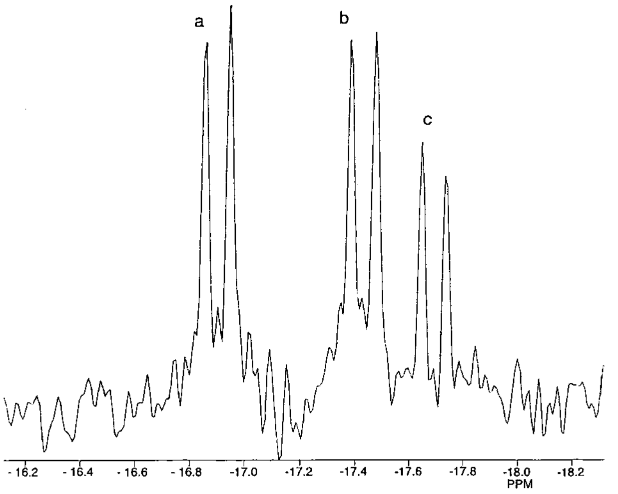

**Figure 11.** $^2H\{^1H\}$ NMR spectrum: (a) **8**, (b) **2b**-hyd$_{d_1}$, (c) **2a**-hyd$_{d_1}$.

The equilibrium constant, $K_{eqH/D}$, for the deuterium-scrambling reaction as written in eq 13 was determined by careful integration of the $^{31}P\{^1H\}$ NMR resonances for the hydride compounds **2a,b**-$\alpha_{d_1}$ and the deuteride compounds **2a,b**-hyd$_{d_1}$ after the deuterium-scrambling reaction reached equilibrium. Quantitative rate data for the deuterium-scrambling process was obtained from the first-order log plots of the disappearance of the hydride signal in the $^1$H NMR spectrum. The equilibrium concentration value, [Hyd]$_{eq}$, was determined from the initial hydride concentration and the equilibrium constant $K_{eqH/D}$ as shown in eq 14. The deuterium-scrambling reaction was separated from the diastereomer interconversion reaction by using the sum of the hydride resonances for **2a** and **2b** for the first-order log plot. The data could be corrected to account for the loss of material to compound **8** by adding 1/9 of the $PMe_3$ integration for **8** to the difference $[\mathrm{Hyd}]_{eq} - [\mathrm{Hyd}]_t$. The first-order log plot is shown in Figure 12. From the observed rate constant for the deuterium scrambling, $k_{obsH/D}$, and the equilibrium constant, $K_{eqH/D}$, the first-order rate constants for the forward, $k_4$, and reverse, $k_{-4}$, reactions could be determined. These rate data are summarized in Table 4.

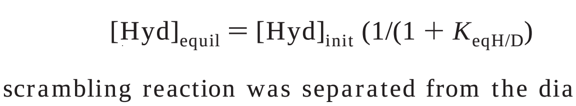

(13)

$$[\mathrm{Hyd}]_{equil} = [\mathrm{Hyd}]_{init}\,(1/(1 + K_{eqH/D}) \qquad (14)$$

## Discussion

Three reactive processes of **2a** and **2b** have been explored in this mechanistic study. The reaction leading to the thermodynamically most stable products is the full reductive elimination of dimethylcyclopropane and the subsequent oxidative addition of $C_6D_6$ to form **8**. This reaction is also the slowest with a rate constant $k_1$ = (1.8 ± 0.8) × $10^{-6}$ $s^{-1}$ at 140 °C. The other two essentially thermoneutral processes observed are approximately 3 times faster in rate. One of these is the equilibration of the two diastereomers, **2a** and **2b**, and the other is the scrambling of isotopic labels between

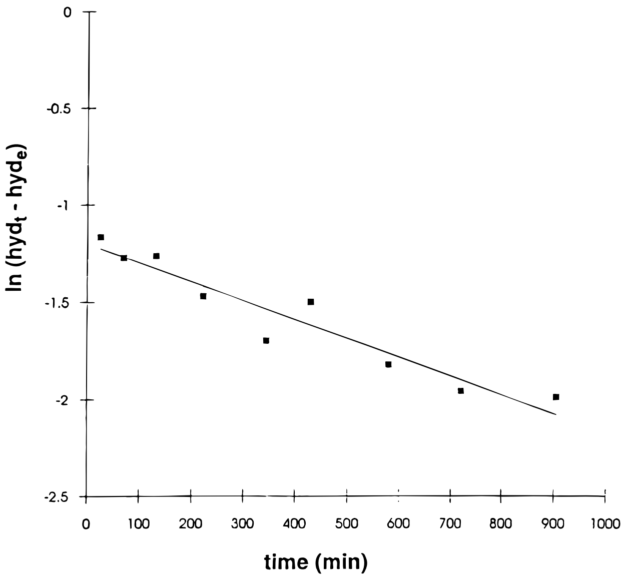

**Figure 12.** First-order log plot for the disappearance of the hydride signal during the thermolysis of (±)-**2a**-$\alpha_{d_1}$. $[\mathrm{Hyd}]_t - [\mathrm{Hyd}]_e$ is the sum of the hydride integrations for **2a** and **2b** at time *t* ($[\mathrm{Hyd}]_t$), less the equilibrium value of the hydride integrations ($[\mathrm{Hyd}]_e$), as determined by the initial hydride integration and the known equilibrium constant ($K_{\mathrm{eqH/D}} = 0.47$, Table 3). This value ($[\mathrm{Hyd}]_t - [\mathrm{Hyd}]_e$) is further corrected for the loss of hydride due to the formation of **8** (see text).

### Scheme 3

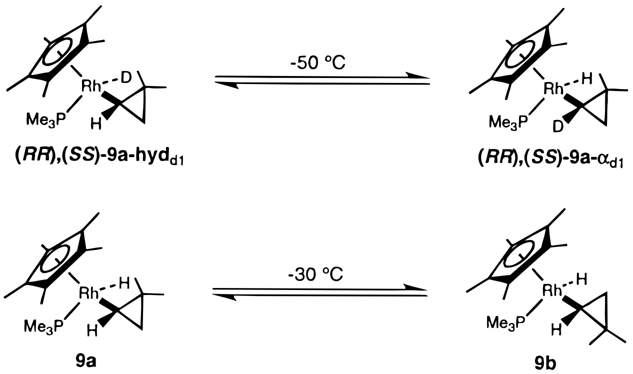

the hydride position and the α-position of the dimethylcyclopropyl group.

The full reductive elimination/oxidative addition[1,3] and the deuterium-scrambling reactions[32−34,44] have many precedents, as outlined in the Introduction. The equilibration of diastereomeric alkylmetal hydrides is also well-known.[1,3] A very close precedent[43] exists in the dimethylcyclopropylrhodium hydride complexes, **9a,b**, studied earlier in our group (Scheme 3). However, there are notable differences between the behavior of the rhodium and iridium systems, outlined below, which lead to some interesting conclusions.

Periana and Bergman synthesized **9a,b** with an excess of one of the diastereomers. They were also able to place a deuterium label in the hydride position of both complexes. However, the thermal instability of the complexes precluded isolation and stereochemical characterization of the compounds. In contrast, the much higher thermal stability of the iridium complexes has allowed us to isolate and fully characterize both **2a** and **2b** in diastereomerically pure form. This characterization includes the determination of the relative stereochemistry of the two diastereomers (see above).

The rate constants for the reductive elimination/oxidative addition, diastereomer interconversion, and deuterium-scrambling reactions of **2a,b** are summarized in Table 4. The rate constants determined by regression analysis for kinetic model A for the diastereomer interconversion can be directly compared to the rate constants for the deuterium-scrambling reactions. The rates of diastereomer interconversion and deuterium scrambling are essentially the same (except for a minor $^2$H isotope effect), and both are faster than that of the full reductive elimination/oxidative addition process. The rhodium system behaves differently. Although the high reactivity of the rhodium system prevented quantitative kinetic analysis, Periana and Bergman found that **9a,b** undergoes isotopic label scrambling at −50 °C yet diastereomer interconversion between **9a** and **9b** occurs much more slowly below −30 °C (Scheme 3).

To examine the differences between these two systems carefully, we must first discuss the mechanisms by which these rearrangements could be occurring. One mechanism that can account for the deuterium-scrambling reactions observed is the dyotropic mechanism depicted in Scheme 4. In this mechanism there is a single symmetrical four-centered transition state. As can be seen in Scheme 4, the expected 1,2-dyotropic transition state results in simultaneous inversion of stereochemical configuration at both the metal and the carbon centers. Although one can imagine a transition state that does not invert both centers, the geometrical constraints of such a transition state make it highly improbable. Because the dyotropic rearrangement results in the concerted inversion of both stereocenters, it cannot be responsible for the diastereomer interconversion observed in either the iridium or the rhodium systems.

Diastereomer interconversion *can* be explained by invoking a mechanism involving alkane complex intermediates. This mechanism is explicitly drawn in Scheme 5 for one enantiomer of **2a** ($S_{\mathrm{Ir}}S_{\mathrm{C}}$) using an alkane complex model with an end-on C−H to metal interaction. In this mechanism, ($S_{\mathrm{Ir}}S_{\mathrm{C}}$)-**2a** undergoes reductive elimination of dimethylcyclopropane (with retention of stereochemical configuration at carbon) to form an intermediate alkane complex, (pro-$S_{\mathrm{Ir}}S_{\mathrm{C}}$)-**10a**, which is in fast equilibrium with the diastereomeric alkane complex (pro-$R_{\mathrm{Ir}}S_{\mathrm{C}}$)-**10b**.[51] Alkane complex (pro-$S_{\mathrm{Ir}}S_{\mathrm{C}}$)-**10a** can be converted to alkane complex (pro-$R_{\mathrm{Ir}}S_{\mathrm{C}}$)-**10b** by a simple 180° rotation about the Ir−H linkage. Reinsertion into the C−H bond by the iridium center generates diastereomer ($R_{\mathrm{Ir}}S_{\mathrm{C}}$)-**2b**. The deuterium-scrambling process can also be explained by the alkane-complex mechanism (Scheme 6). Starting from ($S_{\mathrm{Ir}}R_{\mathrm{C}}$)-**2b**-$\alpha_{d_1}$, reductive elimination forms (pro-$S_{\mathrm{Ir}}R_{\mathrm{C}}$)-**10b**-$_{d_1}$. The iridium center can then “switch” between the C−H

---

(51) In the alkane complex, the iridium center now acts as a prochiral center. To facilitate the discussion: (a) we assume the three atoms, P, Ir, and H (of the alkane ligand), are coplanar with the centroid of the cyclpentadienyl ring; (b) we have arbitrarily defined the direction of insertion of the iridium center into the C−H bond to always proceed toward the second, unbound C−H bond of the alkane ligand; (c) when defining the priority of the C center for stereochemical (*R*,*S*) assignments, the H bound to the iridium has the highest priority; this prevents changing of *R* and *S* designation solely due to changes in priority. Note that this is *not* the accepted system for priority.

**Scheme 4**

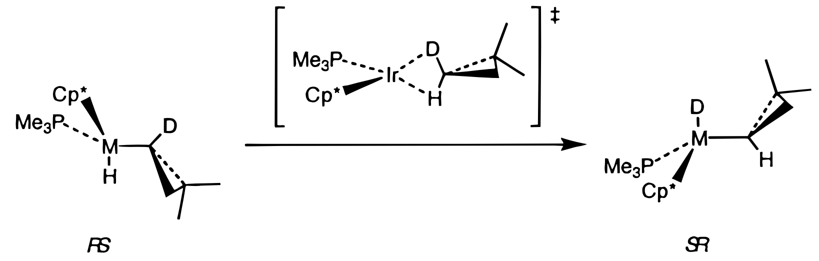

**Scheme 5**

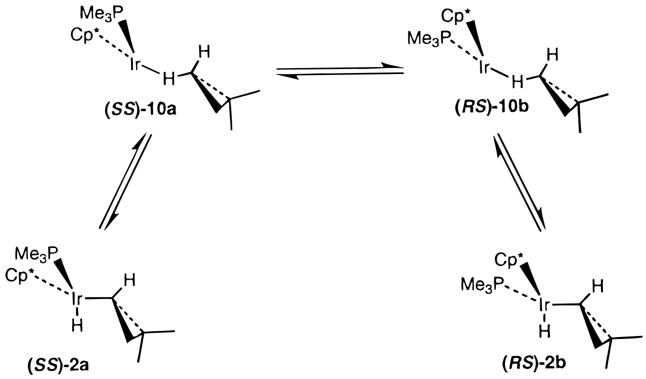

**Scheme 6**

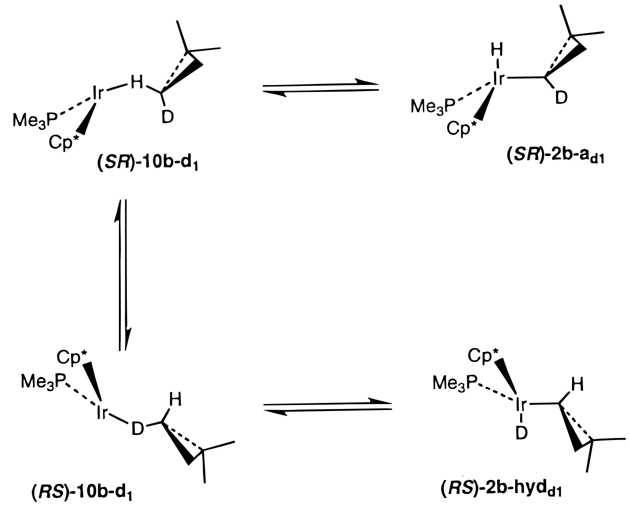

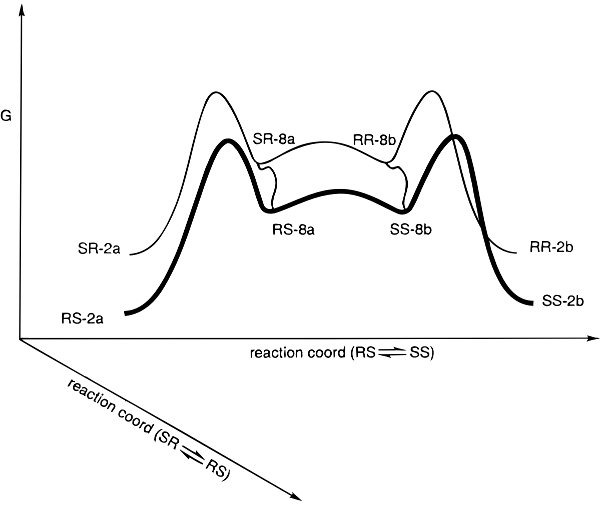

**Figure 13.** Possible reaction energy surface for Scheme 7.

and C−D bonds to form (pro-$R_{\text{Ir}}S_{\text{C}}$)-**10b**-$d_1$. Insertion of the iridium center into the C−D bond produces ($R_{\text{Ir}}S_{\text{C}}$)-**2b**-hyd$_{d_1}$, which is inverted at both iridium and carbon relative to the ($S_{\text{Ir}}R_{\text{C}}$)-**2b**-$\alpha_{d_1}$ complex.

The mechanisms depicted in Schemes 5 and 6 are combined in Scheme 7. In summary, once the alkane complex **10a** or **10b** has been generated, two "alkane complex rearrangement" processes are available: (1) Cp*IrPMe$_3$ rotation resulting in diastereomer interconversion (e.g. **10a** → **10b**) or (2) metal C−H bond "switching" resulting in enantiomer interconversion (e.g. (pro-$R_{\text{Ir}}S_{\text{C}}$)-**10a** → (pro-$S_{\text{Ir}}R_{\text{C}}$)-**10a**) and, in the case of labeled material, isotopic scrambling. This mechanism explains the kinetics observed (the rate of diastereomer interconversion equals the rate of deuterium scrambling) as long as the barriers between **10a** (pro-$R_{\text{Ir}}R_{\text{C}}$), **10a** (pro-$S_{\text{Ir}}S_{\text{C}}$), **10b** (pro-$R_{\text{Ir}}S_{\text{C}}$), and **10b** (pro-$S_{\text{Ir}}R_{\text{C}}$) are all lower than the barrier for reinsertion into the C−H (C−D) bond. We have attempted to provide a graphical illustration of this energetic and mechanistic hypothesis in Figure 13.

As noted earlier, the rhodium system (**9a,b**) behaves differently. An important distinction between the rhodium and iridium systems is the difference in the temperatures at which these reactions occur. Since the rhodium reactions occur at temperatures substantially below 0 °C, small differences in activation energies are easily detected. The high Boltzmann energy associated with the higher temperatures required for the iridium system will mask small differences in activation energies. For the rhodium system, the rate of deuterium-label scrambling is faster than the rate of diastereomer interconversion. One explanation for this difference is that the rhodium rearrangements take place by two different mechanisms: (1) deuterium scrambling is effected by a dyotropic mechanism, whereas (2) diastereomer interconversion occurs by an alkane-complex intermediate mechanism. However, a more economical explanation is that the alkane-complex intermediate mechanism is operational in the rhodium system but the relative barrier heights for C−H bond "switching" (isotopic scrambling, enantiomer interconversion), (Cp*)-Ir(PMe$_3$) fragment rotation (diastereomer interconversion), and C−H bond insertion are different than in the iridium system. Specifically, in the rhodium system, diastereomer interconversion is a higher energy process than enantiomer interconversion and, importantly, it is also a higher energy process than C−H bond insertion. In the iridium system, diastereomer interconversion and enantiomer interconversion are both lower energy processes than C−H bond insertion.

Explanation 2 given above leads to intriguing conclusions regarding the possible structures for the interme-

**Scheme 7**

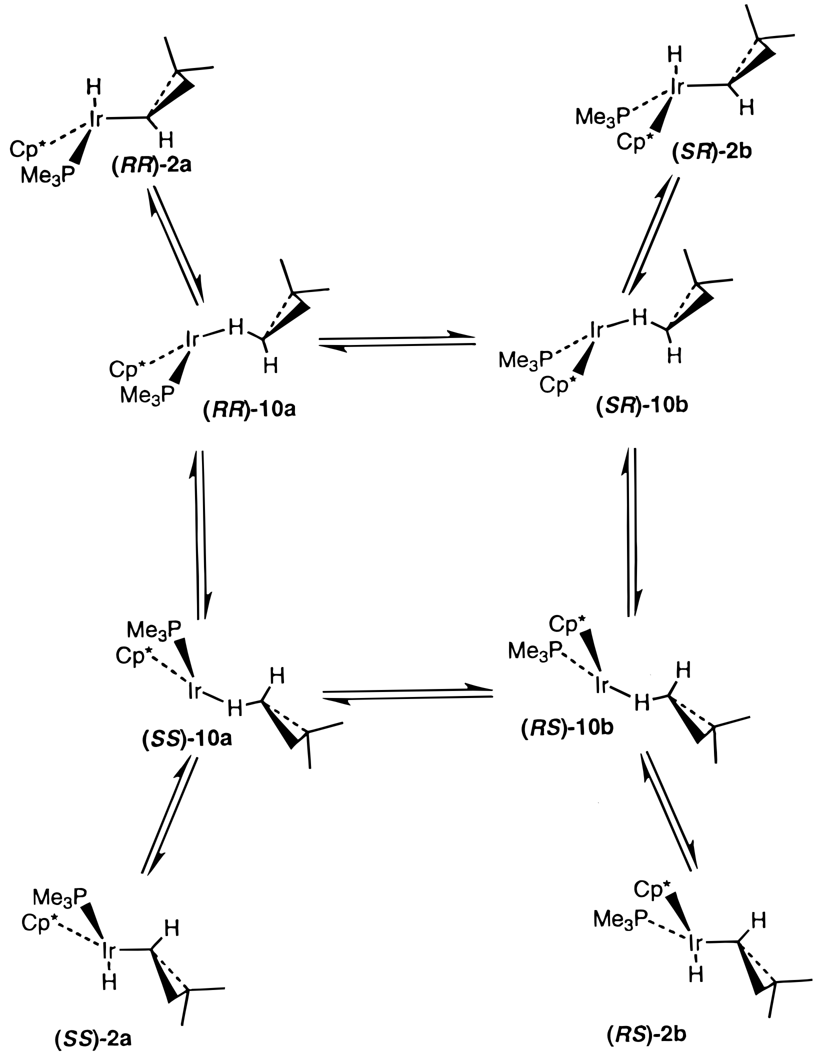

diate iridium and rhodium alkane complexes. Several theoretical studies have predicted various structures for these species. The structures that have received the most theoretical support for the CpML (M = Rh, Ir) system under study here are the side-on $\eta^2$-C,H structure[24] (a in Figure 2) and the end-on $\eta^1$-C,H structure[30,40] (b in Figure 2). Theoretical calculations[23,29,31,40] for the related rhodium and iridium systems $L_2MCl$ (M = Rh, Ir; L = $PH_3$) have predicted that the most stable alkane complex is the chelated $\eta^2$-H,H structure (c in Figure 2). A similar structure for the CpML system was examined in the Morokuma paper[30] and was predicted to be less than 1 kcal/mol higher in energy than the $\eta^1$-H structure; however, the $\eta^2$-H,H structure is not a minimum on the energy surface, and upon minimization, this species rearranged spontaneously to the more stable $\eta^1$-H structure.

The theoretical studies summarized above provide a framework for interpretation of the results described here and those reported earlier by Periana and Bergman. In the $\eta^1$-H structures predicted by Ziegler[40] and Morokuma,[30] the interaction of the H−C bond with the metal center is axially symmetric and, thus, rotation of the CpML fragment should have a small electronic barrier. However, the switching between C−H bonds would proceed through the $\eta^2$-H,H structure, which is predicted to be higher in energy and thus would have a higher electronic barrier to reaction. In contrast, the structure of the $\eta^2$-C,H alkane complex predicted by Hall's calculations[24] has orbital interactions between $\pi$-symmetry as well as $\sigma$-symmetry orbitals. Thus, rotation of the CpML fragment would result in a loss of the $\pi$-symmetry interaction and give rise to an electronic barrier. This structure would also have a barrier for C−H bond switching. The $\eta^2$-H,H alkane complex would not have a barrier to C−H bond switching but would still have a barrier to CpML rotation.

Because the rhodium system experimentally shows a higher barrier for diastereomer interconversion than deuterium scrambling, a structure for the alkane complex which would have a higher barrier for diastereomer interconversion is required. The $\eta^2$-C,H structure for the CpML system, which should have barriers for both diastereomer interconversion and C−H bond switching, is a likely structure for the rhodium intermediate. A structure such as the $\eta^2$-H,H structure predicted for the $L_3RhCl$ fragment by Morokuma and Ziegler is another. This structure would predict that the barrier for C−H bond switching is the same as that for C−H bond oxidative addition, whereas the diastereomer interconversion would require an additional barrier. Thus, the $\eta^2$-C,H structure or the chelating $\eta^2$-H,H structures best explain the qualitative rate behavior seen in the rhodium system. Because the iridium system shows no difference in the rates of diastereomer interconversion and deuterium scrambling, we cannot determine which of the two possible alkane complexes is more likely.

## Conclusion

Due to the similarity of rates for deuterium-scrambling and diastereomer interconversion in the iridium complexes, **2a**, **2b**, **2a**-$\alpha_{d_1}$, and **2b**-$\alpha_{d_1}$, we believe that these two processes are closely related and occur by an alkane-complex intermediate mechanism (Scheme 7). We propose that this mechanism involves the reductive elimination of dimethylcyclopropane, without loss of the alkane into solution, to form the intermediate complexes **10a,b** (or **10a,b**-$d_1$), which are all in rapid equilibrium. Oxidative addition by the metal center into the C−H (or C−D) bond from the four **10a,b** (or **10a,b**-$d_1$) intermediates leads to the enantiomeric pairs of (*RR*),-(*SS*)-(±)-**2a** and (*RS*),(*SR*)-(±)-**2b** (**2a,b**-$\alpha_{d_1}$). Displacement by an external solvent molecule (benzene) irreversibly leads to the stable phenyl hydride oxidative addition product Cp*($PMe_3$)Ir(Ph)(H).

Comparison of the kinetics from the iridium system and the qualitative rate data from the previously studied rhodium system with respect to this mechanism yields the following interesting result. In the iridium system, deuterium scrambling and diastereomer interconversion occur at the same rate, whereas in the rhodium system, the deuterium-scrambling reaction occurs at a lower temperature (faster rate) than the diastereomer scrambling. The nature of the structures of the proposed alkane complexes was discussed with the conclusion that the results of the rhodium thermolyses are better explained by invoking either the $\eta^2$-H,H or $\eta^2$-C,H structures which involve $\pi$-symmetry bonding with the metal center. The results from the thermolyses of the iridium complexes do not differentiate between the possible alkane complexes. This could be due to an inherent difference between the iridium and the rhodium systems; however, due to the high temperatures required for the thermolytic studies of the iridium system, small differences in activation energy are unlikely to be detectable. Further research investigating the nature of alkane complexes and the rearrangements thereof is required to explain the differences between the two systems. In particular, theoretical investigations that examine the reaction trajectories and barriers for interconversion for alkane complexes would be interesting.

## Experimental Section

**General.** Unless otherwise specified, all manipulations were carried out under an inert atmosphere in a Vacuum Atmospheres 553-2 drybox with attached MO-40-2 Dritrain or by using standard Schlenk or vacuum line techniques. Glass reaction vessels fitted with ground glass joints and Teflon high-vacuum stopcocks are referred to as bombs. Glassware was dried at 150 °C before use.

All $^1$H NMR spectra were obtained on commercial Bruker 300-, 400-, or 500-MHz Fourier transform spectrometers at the University of California−Berkeley (UCB) NMR Facility and referenced to residual protiated solvent. All $^{13}C\{^1H\}$, $^{31}P\{^1H\}$, and $^2H\{^1H\}$ NMR spectra were obtained using the same instruments. In cases where assignment of $^{13}C\{^1H\}$ resonances was ambiguous, resonances were assigned using standard DEPT (distortionless enhancement by polarization transfer) sequences.

IR spectra were obtained on a Mattson Galaxy Series FTIR 3000 spectrometer at 4 cm$^{-1}$ resolution. Mass spectrometric (MS) analyses were obtained at the UCB mass spectrometry facility using electron-ionization (EI) or fast-atom bombardment (FAB) techniques. Elemental analyses were obtained from the UCB Microanalytical facility on a Perkin-Elmer 2400 Series II CHNO/S Analyzer. Sealed NMR tubes were prepared using Wilmad 505-PP and 504-PP tubes attached by Cajon adapters directly to Kontes vacuum stopcocks and flame-sealed under reduced pressure.

Photolyses were carried out using a 450 W medium-pressure Hanovia mercury lamp in a double-jacketed quartz immersion well. This apparatus was placed in a 4 L Dewar flask filled with a $H_2O$/ethylene glycol mixture or methanol, which was cooled externally by a Neslab ULT-80DD circulating bath.

Thermolyses were carried out in a Neslab EX-250 HT high-temperature bath filled with Dow Corning 210 H fluid. The temperature was determined using a calibrated Barnant electronic thermocouple (model No. 600-2810). Heating of NMR tubes containing highly volatile solvents (e.g., dimethylcyclopropane) was executed with the use of a cylindrical steel jacket equipped with an O-ring-sealed rupture disk screw top. The flame-sealed NMR tube was inserted into the steel jacket tube, and the remainder of the volume in the steel jacket was filled with a volatile solvent ($Et_2O$ or pentane) to equalize pressure on the NMR tube. The steel jacket was then closed with the rupture disk screw top and the sample thermolyzed.

Low-temperature chromatography was accomplished using doubly jacketed columns. An inner jacket allowed passage of a cooling medium (gaseous $N_2$ passed through liquid $N_2$) to chill the chromatographic support. An outer vacuum jacket provided insulation for the inner jacket. The columns were fitted with a Schlenk inlet to the solvent bulb and a greaseless Teflon stopcock at the base of the column. *Due to the fragility of the glass seals involved in the manufacture of these columns and the large temperature changes to which they are subjected, it is absolutely necessary to wrap the columns with strong tape to prevent shattering in the case of destructive implosions.* Additionally, appropriate face and eye protection should be worn whenever working with the column.

Unless otherwise specified, all reagents were purchased from commercial suppliers and used without subsequent purification. Diethyl ether, THF, pentane, and benzene were distilled from sodium/benzophenone ketyl under nitrogen. Hexanes were distilled from sodium/benzophenone ketyl and tetraglyme under nitrogen. Toluene was distilled from sodium metal under nitrogen. Dimethylcyclopropane was dried over 3 Å molecular sieves and degassed by application of 3 freeze−pump−thaw cycles. (Cp*)($PMe_3$)Ir$(H)_2$ (**1**) and (Cp*)($PMe_3$)-Ir$(OTf)_2$ were prepared by previously reported literature procedures.[5,52] The lithium salts, $Li(CXCH_2C(CH_3)_2)\cdot LiBr$, where X = H or D, were prepared from the corresponding 1-bromo-2,2-dimethylcyclopropane by literature methods.[53]

**Syntheses of Alkyliridium Hydride Complexes.** The photolytic synthesis of **2a,b** is outlined below. The procedures for this synthesis and purification by low-temperature (−80 °C) chromatography to obtain diastereomerically pure material are outlined below for the deuterium-labeled complexes **2a**-$\alpha_{d_1}$ and **2b**-$\alpha_{d_1}$. The syntheses of **2a,b** as described in eq 6 and eq 7 were performed in a manner similar to that used for

---

(52) Stang, P. J.; Huang, Y.; Arif, A. M. *Organometallics* **1992**, *11*, 231.

(53) The lithium salts were prepared by reduction of the bromide with elemental lithium.[57] The bromides were prepared by selective monoreduction of the dibromide with $Bu_3SnX$ (X = H, D).[58] The $Bu_3$-SnD was prepared by reduction of $Bu_3SnCl$ with $LiAlD_4$.[59] The dibromide was prepared from the reaction of isobutylene with dibromocarbene generated in situ by reaction of bromoform with potassium *tert*-butoxide.[60]

the deuterated materials, and so explicit procedures are not included. Spectral data and yields are given for all four compounds.

**(Cp*)(PMe$_3$)Ir(H)[CHCH$_2$C(CH$_3$)$_2$] (2a,b).** Two medium-walled NMR tubes were each charged with 38 mg (0.094 mmol) of (Cp*)(PMe$_3$)Ir(H)$_2$ (**1**).[5] On a high-vacuum line, 1,1-dimethylcyclopropane (0.7 mL) was vacuum transferred to each of the NMR tubes, which were then sealed under vacuum. The tubes were irradiated side-by-side for 24 h at 30 °C to give approximately 80% (by $^{31}$P{$^1$H} NMR analysis) of a mixture of **3**, **2a**, and **2b**. To convert **3** into **2a,b**, the tubes were heated to 135 °C for 3 days. (**CAUTION:** To decrease the danger of these high-pressure thermolyses, the NMR tubes were placed in steel jackets as described above in the general Experimental Section.) The tubes were then opened under vacuum, the solvent was evaporated, and the samples were combined.

**(Cp*)(PMe$_3$)Ir(H)[CDCH$_2$C(CH$_3$)$_2$] (2a,b-$\alpha_{d_1}$).** LiBr (155 mg, 1.79 mmol) was added to a light orange suspension[52] of 600 mg (0.86 mmol) of (Cp*)(PMe$_3$)Ir(OTf)$_2$ in 40 mL of Et$_2$O. This reaction mixture was stirred for 20 min to give a fine, bright orange suspension ((Cp*)(PMe$_3$)IrBr$_2$). The reaction vessel was then placed in a dry ice/acetone low-temperature bath, and a solution of 250 mg (1.3 mmol)[53] of Li(CDCH$_2$C(CH$_3$)$_2$)·LiBr in 2 mL of Et$_2$O was added by syringe techniques to the reaction mixture over a 3 min period. The reaction mixture was warmed to room temperature and stirred for 1 h, producing a translucent orange solution. LiAlH$_4$ (120 mg, 3.2 mmol) was dissolved in 2 mL of Et$_2$O and filtered to remove insoluble material. This LiAlH$_4$ solution was added to the iridium reaction solution by syringe. The reaction vessel was protected from adventitious light by wrapping it in aluminum foil, and the solution was stirred overnight, resulting in a light yellow solution. The solution was then transferred to a bomb, and this vessel was taken into an inert atmosphere box. The reaction solution was chilled to −40 °C in the freezer. A 100 mL, medium porosity frit was loaded with 20 g of dried silica gel and wetted with cold Et$_2$O (−40 °C). The reaction solution was then vacuum-filtered quickly through the silica gel, and the silica gel was washed thoroughly with cold Et$_2$O (−40 °C). The solvent was evaporated in vacuo from the light yellow filtrate to give 250 mg of a highly viscous orange oil. Analysis by $^1$H NMR indicated that the oil was primarily **2a,b**-$\alpha_{d_1}$ (batch A). This procedure was repeated to give approximately 230 mg of **2a,b**-$\alpha_{d_1}$ contaminated with approximately 15% of (Cp*)(PMe$_3$)Ir(H)$_2$ (batch B).

**Low-Temperature Chromatography of (Cp*)(PMe$_3$)Ir(H)[CDCH$_2$C(CH$_3$)$_2$] (2a,b-$\alpha_{d_1}$).** The orange oil from the preparation described above (batch A) was purified by low-temperature chromatography. A 1.7 cm diameter low-temperature chromatography column was loaded with neutral alumina III chromatographic support to produce a column of 50 cm length. The column was evacuated gently and flushed with dry Ar (3×) to provide an oxygen-free atmosphere. The addition of 200 mL of a 5% Et$_2$O/pentane solvent mixture to the dry column by cannula transfer resulted in a highly irregularly packed column. The column was then cooled by passing gaseous nitrogen through liquid nitrogen and then through the inner jacket of the low-temperature column. The column was allowed to equilibrate for a 4 h period; contraction of the solvent during the cooling period resulted in a very tightly packed column. The temperature of the solvent well at the top of the column was −80 °C at the end of the equilibration period. The solvent level was lowered to the level of the chromatographic support, and a 25% Et$_2$O/pentane solution (precooled to dry ice/acetone temperature in a cooling bath) of the orange oil (**2a,b**-$\alpha_{d_1}$) was loaded onto the column using cannula transfer techniques. This solution was drawn onto the column and eluted initially with 2 × 3 mL portions of prechilled (dry ice/acetone) 5% Et$_2$O/pentane eluant. The material was then eluted with 500 mL of 5% Et$_2$O/pentane eluant. Sixteen fractions were collected: fraction 1 and fraction 16 were 150 and 250 mL, respectively; fractions 2−15 were between 25 and 50 mL in volume. Analysis of the fractions (after removal of solvent by evaporation) by $^1$H NMR spectroscopy showed that fractions 4−6 contained mostly **2b**-$\alpha_{d_1}$ (130 mg) and fractions 7−10 contained mostly **2a**-$\alpha_{d_1}$ (40 mg). A second column was run on batch B, giving similar results. The like fractions were combined, and two more columns were run to finally give 51.9 mg of crystalline **2b**-$\alpha_{d_1}$ (0.110 mmol, 7%) and 37.7 mg of the colorless, oily **2a**-$\alpha_{d_1}$ (0.080 mmol, 5%).

**(*RR*),(*SS*)-(±)-(Cp*)(PMe$_3$)Ir(H)[CDCH$_2$C(CH$_3$)$_2$] (2a-$\alpha_{d_1}$).** Pale yellow oil. $^1$H NMR (400 MHz, C$_6$D$_6$): $\delta$ 1.89 (15H, d, $J$ = 1.8 Hz, C$_5$Me$_5$), 1.61 (3H, s, Me$_{\mathrm{cis}}$), 1.51 (3H, s, Me$_{\mathrm{trans}}$), 1.26 (9H, d, $J$ = 9.9 Hz, PMe$_3$), 0.8 (1H, br s, H$_{\beta\mathrm{cis}}$), α-proton resonance not observed, −0.08 (1H, br s, H$_{\beta\mathrm{trans}}$). $^2$H{$^1$H} NMR (61 MHz, C$_6$D$_6$): $\delta$ 0.6 (br s, H$_\alpha$). $^{13}$C{$^1$H} NMR (100 MHz, C$_6$D$_6$): $\delta$ 92.48 (d, $J_{\mathrm{P-C}}$ = 3.3 Hz, $\eta^5$-Me$_5$*C*$_5$), 31.58, 28.93 (2s, CH$_3$), 28.15 (d, $J_{\mathrm{P-C}}$ = 4.3 Hz, CH$_2$), 19.83 (d, $J_{\mathrm{P-C}}$ = 36.1 Hz, PMe$_3$), 18.14 (d, $J_{\mathrm{P-C}}$ = 4.3 Hz, ring quaternary), 10.75 ($\eta^5$-*Me*$_5$C$_5$), α-carbon resonance not observed. $^{31}$P{$^1$H} NMR (162 MHz, C$_6$D$_6$): $\delta$ −42.8. IR (KBr, cm$^{-1}$): 2104 (s, Ir−H stretch), 2156 (sh, C−D stretch).

**(*RS*),(*SR*)-(±)-(Cp*)(PMe$_3$)Ir(H)[CDCH$_2$C(CH$_3$)$_2$] (2b-$\alpha_{d_1}$).** White fluffy powder. $^1$H NMR (400 MHz, C$_6$D$_6$): $\delta$ 1.86 (15H, d, $J$ = 2.0 Hz, C$_5$Me$_5$), 1.45 (3H, s, Me$_{\mathrm{cis}}$), 1.30 (3H, s, Me$_{\mathrm{trans}}$), 1.25 (9H, d, $J$ = 9.8 Hz, PMe$_3$), 0.9 (1H, br s, H$_{\beta\mathrm{cis}}$), α-proton resonance not observed, 0.04 (1H, br s, H$_{\beta\mathrm{trans}}$), −17.57 (1H, d, $J_{\mathrm{P-H}}$ = 10 Hz, Ir−H). $^2$H{$^1$H} NMR (61 MHz, C$_6$D$_6$): $\delta$ 0.6 (br s, H$_\alpha$). $^{13}$C{$^1$H} NMR (100 MHz, C$_6$D$_6$): $\delta$ 92.24 (d, $J_{\mathrm{P-C}}$ = 3.7 Hz, $\eta^5$-Me$_5$*C*$_5$), 29.92, 29.38 (2s, CH$_3$), 23.40 (d, $J_{\mathrm{P-C}}$ = 4.3 Hz, CH$_2$), 19.68 (d, $J_{\mathrm{P-C}}$ = 36.5 Hz, PMe$_3$), 16.46 (s, ring quaternary), 10.44 ($\eta^5$-*Me*$_5$C$_5$), α-carbon resonance not observed. $^{31}$P{$^1$H} NMR (162 MHz, C$_6$D$_6$): $\delta$ −43.8. IR (KBr, cm$^{-1}$): 2140 (s, Ir−H stretch), 2156 (sh, C−D stretch).

**(*RR*),(*SS*)-(±)-(Cp*)(PMe$_3$)Ir(H)[CHCH$_2$C(CH$_3$)$_2$] (2a).** White fluffy powder. $^1$H NMR (400 MHz, C$_6$D$_6$): $\delta$ 1.86 (15H, d, $J$ = 2.0 Hz, C$_5$Me$_5$), 1.45 (3H, s, Me$_{\mathrm{cis}}$), 1.30 (3H, s, Me$_{\mathrm{trans}}$), 1.25 (9H, d, $J$ = 9.8 Hz, PMe$_3$), 0.87 (1H, dd, $J$ = 9.1, 2.6 Hz, H$_{\beta\mathrm{cis}}$), 0.64 (1H, m, H$_\alpha$), 0.04 (1H, dd, $J$ = 6.6, 2.6 Hz, H$_{\beta\mathrm{trans}}$), −17.57 (1H, d, $J_{\mathrm{P-H}}$ = 10 Hz, Ir−H). $^{13}$C{$^1$H} NMR (100 MHz, C$_6$D$_6$): $\delta$ 92.24 (d, $J_{\mathrm{P-C}}$ = 3.7 Hz, $\eta^5$-Me$_5$*C*$_5$), 29.92, 29.38 (2s, CH$_3$), 23.40 (d, $J_{\mathrm{P-C}}$ = 4.3 Hz, CH$_2$), 19.68 (d, $J_{\mathrm{P-C}}$ = 36.5 Hz, PMe$_3$), 16.46 (s, ring quaternary), 10.44 ($\eta^5$-*Me*$_5$C$_5$), −9.46 (d, $J_{\mathrm{P-C}}$ = 10.6 Hz, α-CH). $^{31}$P{$^1$H} NMR (162 MHz, C$_6$D$_6$): $\delta$ −43.8. IR (KBr): 2140 cm$^{-1}$ (s, Ir−H stretch). MS (EI, 70 eV) *m/z* 474, 472 (8.7, 5.6, M$^+$). Anal. Calcd for C$_{18}$H$_{34}$IrP: C, 45.64; H, 7.23. Found: C, 45.77; H, 7.44.

**(*RS*),(*SR*)-(±)-(Cp*)(PMe$_3$)Ir(H)[CHCH$_2$C(CH$_3$)$_2$] (2b).** Colorless oil. $^1$H NMR (400 MHz, C$_6$D$_6$): $\delta$ 1.89 (15H, d, $J$ = 1.8 Hz, C$_5$Me$_5$), 1.61 (3H, s, Me$_{\mathrm{cis}}$), 1.51 (3H, s, Me$_{\mathrm{trans}}$), 1.26 (9H, d, $J$ = 9.9 Hz, PMe$_3$), 0.78 (1H, dd, $J$ = 9.0, 2.0 Hz, H$_{\beta\mathrm{cis}}$), 0.68 (1H, m, H$_\alpha$), −0.08 (1H, ddd, $J$ = 6.6, 2.0 Hz, $J_{\mathrm{P-H}}$ = 1.8 Hz, H$_{\beta\mathrm{trans}}$), −17.81 (d, $J_{\mathrm{P-H}}$ = 35.7 Hz, Ir−H). $^{13}$C{$^1$H} NMR (100 MHz, C$_6$D$_6$): $\delta$ 92.48 (d, $J_{\mathrm{P-C}}$ = 3.3 Hz, $\eta^5$-Me$_5$*C*$_5$), 31.58, 28.93 (2s, CH$_3$), 28.15 (d, $J_{\mathrm{P-C}}$ = 4.3 Hz, CH$_2$), 19.83 (d, $J_{\mathrm{P-C}}$ = 36.1 Hz, PMe$_3$), 18.14 (d, $J_{\mathrm{P-C}}$ = 4.3 Hz, ring quaternary), 10.75 ($\eta^5$-*Me*$_5$C$_5$), −7.62 (d, $J_{\mathrm{P-C}}$ = 11.4 Hz, α-CH). $^{31}$P{$^1$H} NMR (162 MHz, C$_6$D$_6$): $\delta$ −42.8. IR (KBr): 2104 cm$^{-1}$ (s, Ir−H stretch). HRMS (EI) calcd for C$_{18}$H$_{34}$IrP, 474.2028; found, 474.2031.

**$^1$H−$^1$H NOESY Spectrum of (Cp*)(PMe$_3$)Ir(H)[CHCH$_2$C(CH$_3$)$_2$] (2a,b).** A 1:1 mixture of **2a,b** was prepared by allowing 20 mg (0.036 mmol) of **5a** to react with 3.0 mg (0.079 mmol) of LiAlH$_4$ in 5 mL of Et$_2$O. The sample was then quickly passed through a prechilled (−40 °C) glass pipet column containing 1 g of alumina III wetted with Et$_2$O using prechilled Et$_2$O as the eluant. The Et$_2$O was removed in vacuo to produce a colorless oil. This oil was then dissolved in 0.5 mL of C$_6$D$_6$ and placed in an NMR tube, which was sealed under vacuum. A phase-sensitive (TPPI, time proportional phase incrementation method) $^1$H−$^1$H NOESY spectrum (27

°C) with broad-band $^{31}P$ decoupling (CPD (composite pulse decoupling)) using a GARP (globally-optimized alternating-phase rectangular pulses) sequence was acquired using a Bruker AMX400 instrument. For each of the 128 $T_1$ experiments, 8 scans were averaged, taking 1024 data points with an acquisition time of 0.99 s and a recycle delay of 3.5 s with a mixing time of 1.5 s. A spectral width of 1050 Hz was used. COSY-type artifacts were removed by varying the mixing time (2%) as described by Ernst and co-workers.[54]

**(Cp*)(PMe$_3$)Ir(Br)[CHCH$_2$C(CH$_3$)$_2$] (5a).** A light orange suspension[52] of 736 mg (1.05 mmol) of (Cp*)(PMe$_3$)Ir(OTf)$_2$ in 30 mL of chilled Et$_2$O (−40 °C) was treated with a solution of 390 mg (2.11 mmol) of Li(CHCH$_2$C(CH$_3$)$_2$)·LiBr in 10 mL of chilled Et$_2$O. The reaction mixture was warmed to room temperature and stirred for 15 min, producing a dark orange solution. This solution was vacuum filtered through a bed of SiO$_2$ to quench the excess lithium reagent. The Et$_2$O was removed in vacuo, and the resulting brownish-orange powder was washed with pentane. The remaining solid was then dissolved in toluene and filtered through a bed of Celite to remove brown insoluble material. The material was recrystallized twice from toluene and pentane to give 150 mg (0.272 mmol, 25.9%) of orange crystals. Presumably, higher yields of material could be obtained using the modified procedure for synthesis of **5a** as described in the synthesis of **2a,b**. However, this alternative was not attempted. $^1H$ NMR (400 MHz, C$_6$D$_6$): $\delta$ 1.53 (15H, d, $J = 2.1$ Hz, C$_5$Me$_5$), 1.56, 1.55 (6H, two s, Me$_{cis}$ and Me$_{trans}$), 1.25 (9H, d, $J = 10.4$ Hz, PMe$_3$), 1.05 (1H, m, ring proton), 0.82 (1H, m, ring proton), 0.38 (1H, m, ring proton). $^1H$ NMR (400 MHz, THF-d$_8$): $\delta$ 1.6 (15H, d, $J = 2.1$ Hz, C$_5$Me$_5$), 1.02 (3H, s, Me$_{cis}$), 0.85 (3H, s, Me$_{trans}$), 1.4 (9H, d, $J = 10.4$ Hz, PMe$_3$), 0.55 (1H, m, H$_\alpha$), 0.19 (1H, m, H$_{\beta trans}$), −0.24 (1H, m, H$_{\beta cis}$). $^{13}C\{^1H\}$ NMR (100 MHz, C$_6$D$_6$): $\delta$ 92.31 (d, $J_{P-C} = 3.7$ Hz, $\eta^5$-Me$_5$$C_5$), 33.46, 24.35 (2s, $C$H$_3$), 22.93 (d, $J_{P-C} = 1.2$ Hz, $C$H$_2$), 14.58 (d, $J_{P-C} = 37.6$ Hz, PMe$_3$), 18.93 (s, ring quaternary), 9.03 ($\eta^5$-$Me_5$C$_5$), −1.22 (d, $J_{C-P} = 14.9$ Hz, α-C). $^{31}P\{^1H\}$ NMR (162 MHz, C$_6$D$_6$): $\delta$ −35.6. IR (KBr, cm$^{-1}$): 3039 (w), 2952 (s), 2906 (s), 2715 (w), 1510 (w), 1450 (m), 1377 (m), 1279 (m), 1205 (m), 1155 (w), 1117 (w), 1026 (m), 958 (s), 856 (w), 731 (m), 680 (w), 611 (w).

**X-ray Analysis of (Cp*)(PMe$_3$)Ir(Br)[CHCH$_2$C(CH$_3$)$_2$] (5a).** Dark orange crystals were obtained by slow crystallization from a toluene solution of **5a** layered with pentane. Sample crystals detached from one of these crystals were mounted on glass fibers using Paratone N hydrocarbon oil. The crystal used for data collection was transferred to our Enraf-Nonius CAD-4 diffractometer and centered in the beam. The crystal was quickly cooled to −91 °C by a nitrogen-flow low-temperature apparatus which had been previously calibrated by a thermocouple placed at the sample position. Automatic peak search and indexing procedures yielded a monoclinic reduced primitive cell. Inspection of the Niggli values revealed no conventional cell of higher symmetry. The final cell parameters and specific data collection parameters for this data set are given in Table 2.

The raw intensity data were converted to structure factor amplitudes and their esd's by correction for scan speed, background, and Lorentz and polarization effects. No correction for crystal decomposition was necessary. An empirical correction based on the observed variation was applied to the data, with $T_{max} = 1.23$ and $T_{min} = 0.83$. Inspection of the systematic absences indicated the unique space group $P2_1/n$. Removal of systematically absent and redundant data left 2628 unique data in the final data set.

The structure was solved by Patterson methods and refined via standard least-squares and Fourier techniques. In a difference map calculated following the refinement of all non-hydrogen atoms with anisotropic thermal parameters, peaks were found corresponding to the positions of all of the hydrogen atoms. Hydrogen atomic positions and isotropic thermal parameters were refined. All other atoms were refined with anisotropic thermal parameters.

The final residuals for the 323 parameters were refined against the 2275 data for which $F^2 > 3\sigma$ were $R = 2.15\%$, w$R = 2.57\%$, and GOF = 1.33. The $R$ value for all 2628 data was 2.83%. The quantity minimized by the least-squares program was $\sum w([F_o] - [F_c])^2$, where $w$ is the weight of a given observation. The $p$-factor, used to reduce the weight of intense reflections, was set to 0.03 in the last cycles of the refinement. The analytical forms of the scattering factor tables for the neutral atoms were used, and all scattering factors were corrected for both the real and imaginary components of anomalous dispersion.

Inspection of the residuals ordered in ranges of $\sin\theta/\lambda$, $[F_o]$, and parity and value of the individual indexes showed no unusual features or trends. The largest peak in the final difference Fourier map had an electron density of 0.92 e$^-$/Å$^3$ and the lowest excursion −0.60 e$^-$/Å$^3$.

**$^1H-^1H$ NOESY Spectrum of (Cp*)(PMe$_3$)Ir(Br)[CHCH$_2$C(CH$_3$)$_2$] (5a).** An NMR sample (prepared in the air) containing 12.7 mg (0.023 mmol) of (Cp*)(PMe$_3$)Ir(Br)[CHCH$_2$C(CH$_3$)$_2$] (**5a**) and 100 mg (1.15 mmol) of LiBr in 0.4 mL of THF-$d_8$ was degassed by 4 freeze−pump−thaw cycles and sealed under vacuum. A phase-sensitive (TPPI) $^1H-^1H$ NOESY spectrum (27 °C) with $^{31}P$ decoupling was acquired using a Bruker AMX400 instrument. For each of the 128 experiments, 8 scans were averaged, taking 1024 complex points with an acquisition time of 0.43 s and a relaxation delay of 3.5 s using a mixing time of 1.5 s. A spectral width of 1200 Hz was used. COSY-type artifacts were removed by varying the mixing time (2%) as described by Ernst and co-workers.[54]

**Conversion of (Cp*)(PMe$_3$)Ir(Br)[CHCH$_2$C(CH$_3$)$_2$] (5a) to (Cp*)(PMe$_3$)Ir(Br)[CH$_2$CH=C(CH$_3$)$_2$] (7) by Thermolysis.** (Cp*)(PMe$_3$)Ir(Br)[CHCH$_2$C(CH$_3$)$_2$] (4.4 mg, 0.0080 mmol) and internal standard trimethoxybenzene (1.5 mg, 0.0026 mmol) were dissolved in 0.5 mL of C$_6$D$_6$, placed in an NMR tube, and sealed under vacuum. The sample was thermolyzed for 6 h at 65 °C. Analysis by $^1H$ NMR indicated that 75% of **5a** had been converted to **7**. Isolation and full characterization were not attempted. $^1H$ NMR (400 MHz, C$_6$D$_6$): $\delta$ 5.41 (1H, m, vinyl H), 3.4 (1H, m, allylic H), 2.75 (1H, m, allylic H), 1.78, 1.77 (6H, two s, Me$_{cis}$ and Me$_{trans}$), 1.50 (15H, d, $J = 2$ Hz, C$_5$Me$_5$), 1.27 (9H, d, $J = 10$ Hz, PMe$_3$). $^{13}C\{^1H\}$ NMR (100 MHz, C$_6$D$_6$): $\delta$ 136.8 (d), 122.42 (s), 91.72 (d, $\eta^5$-Me$_5$$C_5$), 26.13, 18.35 (2s, $C$H$_3$), 14.77 (d, PMe$_3$), −1.49 (d, $C$H$_2$). $^{31}P\{^1H\}$ NMR (162 MHz, C$_6$D$_6$): $\delta$ −36.5.

**(Cp*)(PMe$_3$)Ir(H)[CH$_2$C(CH$_3$)CH$_2$CH$_2$] (3).** To a pentane slurry[55] (20 mL) of Li[(Cp*)(PMe$_3$)Ir(H)], prepared from 152 mg (0.375 mmol) of (Cp*)(PMe$_3$)Ir(H)$_2$ and 0.3 mL of a solution of $^t$BuLi in pentane (1.7 M, 0.510 mmol), a solution of (1-methylcyclopropyl)methyl tosylate[56] (127 mg, 0.528 mmol) in 1 mL of benzene was added and the mixture stirred for 48 h at ambient temperature. After evaporation of the solvent, the residue was extracted 3 times with 5 mL of pentane and the combined extracts were filtered through glass wool. After evaporation of the solvent, $^1H$ NMR analysis showed that 29% of **3** had formed in addition to (Cp*)(PMe$_3$)Ir(H)$_2$. Two further runs, carried out in a similar manner, gave 14% and 41% of crude **3**, respectively. Cold chromatography of the combined

---

[54] Macura, S.; Huang, Y.; Suter, D.; Ernst, R. R. *J. Magn. Reson.* **1981**, *43*, 259.

[55] Gilbert, T. M.; Bergman, R. G. *J. Am. Chem. Soc.* **1985**, *107*, 3502.

[56] Kabalka, G. W.; Varma, M.; Varma, R. S.; Srivastava, P. C.; Knapp, F. F., Jr. *J. Org. Chem.* **1986**, *51*, 4814.

[57] Seyferth, D.; Cohen, H. M. *J. Organomet. Chem.* **1963**, *1*, 15.

[58] Seyferth, D.; Yamazaki, H.; Alleston, D. L. *J. Org. Chem.* **1963**, *28*, 703.

[59] Van der Kerk, G. J. M.; Noltes, J. G.; Luijten, J. G. A. *J. Appl. Chem.* **1957**, *7*, 366.

[60] Skell, P. S.; Garner, A. Y. *J. Am. Chem. Soc.* **1956**, *78*, 5430. *J. Org. Chem.* **1986**, *51*, 2386.

samples gave 73 mg (12%) of tan, air-sensitive **3**, which was recrystallized at − 40 °C from methylcyclohexane. $^1$H NMR ($C_6D_6$): $\delta$ 1.88 (d, $J_{P-C} = 12.3$ Hz, α-CHH′), 1.84 (d, $J_{P-H} = 1.9$ Hz, $\eta^5$-$Me_5C_5$), 1.67 (t, $J_{P-C} = J_{11} = 12.6$ Hz, α-CHH′), 1.51 (s, $CH_3$), 1.18 (d, $J_{P-H} = 9.6$ Hz, $PMe_3$), 0.72, 0.57, 0.42, 0.29 (4 ddd, $J_{11} = 2.9$ Hz, $J_{12} = 5.4$ Hz, $J_{12'} = 8.7$ Hz), −17.82 (d, $J_{P-H} = 37.6$ Hz, Ir−H). $^{13}C\{^1H\}$ NMR ($C_6D_6$): $\delta$ 91.59 (d, $J_{P-C} = 3.3$ Hz, $\eta^5$-$Me_5C_5$), 29.39 (s, $CH_3$),18.93 (d, $J_{P-C} = 35.6$ Hz, $PMe_3$), 18.85 (d, $J_{P-C} = 1.4$ Hz, C), 15.88, 14.22 (2 s, $\gamma$-$CH_2$), 10.32 (s, $\eta^5$-$Me_5C_5$), 0.81 (d, $J_{P-C} = 7.2$ Hz, α-$CH_2$). $^{31}P\{^1H\}$ NMR: $\delta$ −42.3. IR (KBr): 2113 (s, $\nu_{Ir-H}$). MS (70 eV): *m/z* 474, 472 (8.7, 5.5, $M^+$), 404 (68), 402 (64), 400 (42), 372 (47), 121 (35), 119 (56), 84 (80), 76 (36), 55 (100). Mp: 50−53 °C. HRMS calcd for $C_{18}H_{34}IrP$, 474.2028, 472.2004; found, 474.2039, 472.1988.

**X-ray Analysis of (Cp*)($PMe_3$)Ir(H)[$CH_2C(CH_3)CH_2CH_2$] (3).** Crystals of **3** suitable for X-ray diffraction were grown from methylcyclohexane at −40 °C and mounted as described above for **5a**. The final cell parameters and specific data collection parameters for this data set are given in Table 2.

The raw intensity data were converted to structure factor amplitudes and their esd's by correction for scan speed, background, and Lorentz and polarization effects. No correction for crystal decomposition was necessary. Inspection of the azimuthal scan data showed a variation $I_{min}/I_{max} = 0.429$ for the average curve. An empirical correction based on the observed variation was applied to the data. Inspection of the systematic absences indicated the unique space group $P2_1/n$. Removal of systematically absent and redundant data left 2514 unique data in the final data set.

The structure was solved by Patterson methods and refined via standard least-squares and Fourier techniques. In a difference map calculated following the refinement of all non-hydrogen atoms with anisotropic thermal parameters, peaks were found corresponding to the positions of most of the hydrogen atoms. Hydrogen atoms were assigned idealized locations and values of $B_{iso}$ 1.3 times the $B_{eqv}$ of the atoms to which they were attached. A peak of height 0.9 $e^-/Å^3$ was located in a difference map prior to final refinement, in a position consistent with the expected position of the hydride ligand. A hydrogen atom was placed at this position and was given a value of 3.0 $Å^2$ for $B_{iso}$. Hydrogen atoms were included in structure calculations but were not refined by least-squares analysis.

The final residuals for the 181 parameters were refined against the 2095 data for which $F^2 > 3\sigma$ were $R = 3.5\%$, w$R$ = 4.4%, and GOF = 1.47. The $R$ value for all 2514 data was 4.5%. The quantity minimized by the least-squares program was $\sum w([F_o] - [F_c])^2$, where $w$ is the weight of a given observation. The *p*-factor, used to reduce the weight of intense reflections, was set to 0.05 in the last cycles of the refinement. The analytical forms of the scattering factor tables for the neutral atoms were used, and all scattering factors were corrected for both the real and imaginary components of anomalous dispersion.

Inspection of the residuals ordered in ranges of sin $\theta/\lambda$, $[F_o]$, and parity and value of the individual indexes showed no unusual features or trends. The largest peak in the final difference Fourier map had an electron density of 1.838 $e^-/Å^3$ and the lowest excursion 2.280 $e^-/Å^3$. Both were located near the Ir. There was no indication of secondary extinction in the high-intensity low-angle data.

**Kinetics of Thermolyses of 2a,b.** The kinetics of the thermolysis of **2a,b** and their deuterated analogues **2a,b**-$\alpha_{d_1}$ were carried out in a constant-temperature bath set at 140 °C. The temperature of the kinetic bath was periodically checked during the thermolysis; it was found to be stable to within 1 °C of the set temperature. Times of thermolyses were monitored using a digital stopwatch. Upon removal of the thermolyzed samples from the kinetic bath, the temperature of the samples was lowered quickly by placing them immediately in a flask of water at room temperature.

The samples of **2a**, **2b**, **2a**-$\alpha_{d_1}$, and **2b**-$\alpha_{d_1}$ were thermolyzed in flame-sealed, thin-walled NMR tubes. Flared, cylindrically symmetric capillary tubes were manufactured to fit snugly into the thin-walled NMR tubes. These capillary tubes were filled with an external standard $C_6D_6$ solution of (Cp*)($PMe_3$)Ir$(H)_2$ (**1**), trimethoxybenzene, and triphenylphosphine (added to prevent exchange of deuterium from the $C_6D_6$ into the hydride positions of **1**). Stock solutions of the complexes were prepared and then used to prepare the NMR samples. A typical kinetic sample preparation is described below.

**External Capillary Standard Preparation.** A standard external capillary solution was prepared by dissolving 35.4 mg (0.0873 mmol) of (Cp*)($PMe_3$)Ir$(H)_2$ (**1**), 5 mg (0.0298 mmol) of trimethoxybenzene, and 1.8 mg (0.00687 mmol) of triphenylphosphine in 180 $\mu$L of $C_6D_6$. A flared capillary was charged with 30.0 $\mu$L of this external capillary standard solution and flame-sealed at liquid $N_2$ temperature under an atmosphere of $N_2$.

**Thermolysis Sample (2a) Preparation.** A standard solution of **2a** was prepared by dissolving 17.2 mg (0.0362 mmol) of pure **2a** in 180 $\mu$L of $C_6D_6$ (0.000201 mmol/$\mu$L). A triphenylphosphine standard solution was prepared by dissolving 3.1 mg (0.012 mmol) of triphenyphosphine in 130 $\mu$L of $C_6D_6$ ($9.08 \times 10^{-5}$ mmol/$\mu$L). The sample solution was then prepared by dissolving 60.0 $\mu$L (0.0121 mmol) of the **2a** standard solution and 15.0 $\mu$L (0.00136 mmol) of the triphenylphosphine standard solution in 440 $\mu$L of $C_6D_6$. This resulted in a solution that is 0.0234 M in **2a** and 0.00264 M in triphenylphosphine. This sample solution was then placed in an NMR tube with the external standard capillary described above, frozen at liquid $N_2$ temperature, and flame-sealed under an atmosphere of $N_2$.

**Kinetics of Thermolysis.** An initial $^1$H NMR spectrum of the sample was taken. The $^1$H NMR spectra for these kinetic studies were single-pulse experiments using an initially calibrated 90° pulse. The samples were allowed to equilibrate in the spectrometer for at least 2 min prior to acquiring the FID to ensure that complete relaxation to the Boltzmann populations had occurred. The NMR tubes were spun to ensure sufficient resolution between the methyl resonances. The NMR sample was then thermolyzed at 140 °C for recorded amounts of time; NMR spectra were acquired at each time period.

After all of the FID data sets were collected, they were all transformed and phased. A base line correction was applied, and the spectra were integrated against the external references (Cp*)($PMe_3$)Ir$(H)_2$ (**1**) and trimethoxybenzene using standardized integration limits chosen from spectra acquired late in the kinetic run. These integration data were transferred to a computer and analyzed as described in the Supporting Information.

**Acknowledgment.** We thank Dr. Fred Hollander, Director of the U.C. Berkeley X-ray Diffraction Facility (CHEXRAY), for determination of the crystal structures of **5a** and **3**. We are grateful for support of this work by the Director, Office of Energy Research, Chemical Science Division, U.S. Department of Energy, under contract no. DE-AC03-76SF00098.

**Supporting Information Available:** Description of kinetic models A and B, equations for derivation of kinetic models A and B, plots of the dihedral minimizations of **5a** and (*RR*)-**2a**, and tables of positional parameters, anisotropic thermal parameters, and selected bond distances and angles for (*RS*)-**5a** and **3** (20 pages). Ordering information is given on any current masthead page.

OM980355F